Effects of Detector Thickness on Geometric Sensitivity and Event Positioning Errors in the Rectangular PET/X Scanner

Journal:	*IEEE Transactions on Nuclear Science*
Manuscript ID:	TNS-00826-2012.R1
Manuscript Type:	Imaging and Instrumentation for Nuclear Medicine
Date Submitted by the Author:	n/a
Complete List of Authors:	MacDonald, Lawrence; University of Washington, Radiology Hunter, William; University of Washington, Dept. of Radiology Kinahan, Paul; University of Washington, Dept. of Radiology Miyaoka, Robert; University of Washington, Radiology
Standard Key Words:	Application specific imagers, PET, Spatial resolution, Simulation

Effects of Detector Thickness on Geometric Sensitivity and Event Positioning Errors in the Rectangular PET/X Scanner

Lawrence R. MacDonald, *Member IEEE*, William C.J. Hunter, *Member IEEE*, Paul E. Kinahan, *Fellow IEEE*, and Robert S. Miyaoka, *Senior Member IEEE*

Abstract- We are investigating a rectangular box PET scanner to be used in conjunction with conventional x-ray mammography for combined breast PET/x-ray mammography imaging. In this study we used Monte Carlo simulations to characterize the tradeoffs between photon sensitivity and event mis-positioning as a function of detector thickness.

Methods: We simulated a four-panel system with two 20 x 15cm and two 10 x 15cm flat detectors forming a box, with the larger detectors separated by 4 cm or 8 cm corresponding to different breast sizes. Coincident-photon sensitivity, scatter fraction, and spatial resolution were studied as a function of scintillation crystal thickness. Detector spatial resolution was modeled anisotropically with fixed 2 mm FWHM lateral resolution, and depth-of-interaction (DOI) resolution depending on crystal thickness. To analyze spatial resolution independently of the image reconstruction algorithm, we derived a projection-based event-positioning metric (d_{FWHM}) from simulated list-mode data.

Results: For an 8 cm thick uniform test object overall system sensitivity increased from 2.6% to 21% as detector thickness increased from 5 mm to 40 mm. Sensitivities increased by approximately 1/3 as detector separation decreased to 4 cm. Our spatial resolution metric, d_{FWHM}, increased from 0.75 mm to 1.8 mm for a central point source in air without DOI information as detector thickness increased from 5 mm to 40 mm. With DOI information included, d_{FWHM} improved by 12% and 29% for 5 mm and 40 mm thick detectors, respectively. For a point source in the corner of the field of view, DOI information improved d_{FWHM} by 20% and 45% for 5 mm and 40 mm detectors. Sensitivity was 7.7% for 10 mm thick crystals (8 cm object). Increasing crystal thickness on the smaller side detectors from 10 mm to 20 mm (keeping 10 mm crystals on the larger detectors) boosted sensitivity by 24% (relative) and degraded d_{FWHM} by only ~3%/8% with/without DOI information.

Conclusions: The close proximity of detectors and object in PET/X means sensitivity similar to whole-body PET scanners can be achieved with 10 mm thick crystals. In such thin crystals, DOI effects, and thus the advantages of measuring DOI, both diminish. The benefits of measuring DOI must be evaluated in terms of the intended clinical task of assessing tracer uptake in small lesions. Increasing crystal thickness on the smaller side detectors provides substantial sensitivity increase with minimal accompanying loss in resolution.

I. Introduction

EVALUATION of new therapies in clinical trials and optimizing individual therapy regimens are two promising applications for dedicated breast PET scanning. We are studying the design of a rectangular box-shaped PET scanner that will attach to an x-ray mammography gantry (PET/X, fig. 1). The goal of this scanner is to enable development and evaluation of new and existing breast cancer therapies by using PET images as prognostic biomarkers. This approach has been used for advanced breast cancer lesions at our institutions [1]-[2] and others [3]-[4]. It has the potential to both streamline development of new therapies, by providing earlier feedback about *in vivo* efficacy, and to optimize existing therapy regimens on an individual patient level by measuring response to neoadjuvant treatments. The use of PET images as a biomarker greatly benefits from quantitative accuracy and reproducibility in measuring tracer uptake. The

Manuscript received 15 Oct. 2012. This work was supported in part by NIH NCI under Grant No. CA134855 and the Coulter Translational

L.R. MacDonald is with the University of Washington Department of Radiology, Seattle, WA, USA (e-mail: macdon@uw.edu).

W.C.J. Hunter is with the University of Washington Department of Radiology, Seattle, WA, USA (e-mail: wcjh@uw.edu).

P.E. Kinahan is with the University of Washington Department of Radiology, Seattle, WA, USA (e-mail: kinahan@uw.edu).

R.S. Miyaoka is with the University of Washington Department of Radiology, Seattle, WA, USA (e-mail: rmiyaoka@uw.edu).

approach is currently limited to locally advanced disease where lesions are large enough for quantitatively accurate assessment with whole-body PET scanners; generally believed to be > 2-3 cm on modern scanners [5]-[6]. This is a significant limitation for the applications mentioned above for two reasons; one is that the majority (~60%) of breast cancer patients are diagnosed with early stage disease, meaning lesions that are less than 2 cm in extent [7], the second is that evaluating efficacy of new therapies is preferably done in the setting of less de-differentiated tumors, i.e. early-stage tumors that have undergone fewer mutations from the biochemistry of the originating disease. Several dedicated breast PET systems have been built or are under development [8-19]; the design we are pursuing resembles the four-sided flat panel geometry developed at the Lawrence Berkeley National Laboratory [11]. As part of that work, Qi et al. [20] suggested a four-sided system with depth-of-interaction (DOI) capability is needed to optimize both lesion detection and quantification tasks. Such a dedicated scanner would enable high geometric sensitivity through proximity to the source object, but it is also susceptible to significant event mis-positioning due to detection parallax.

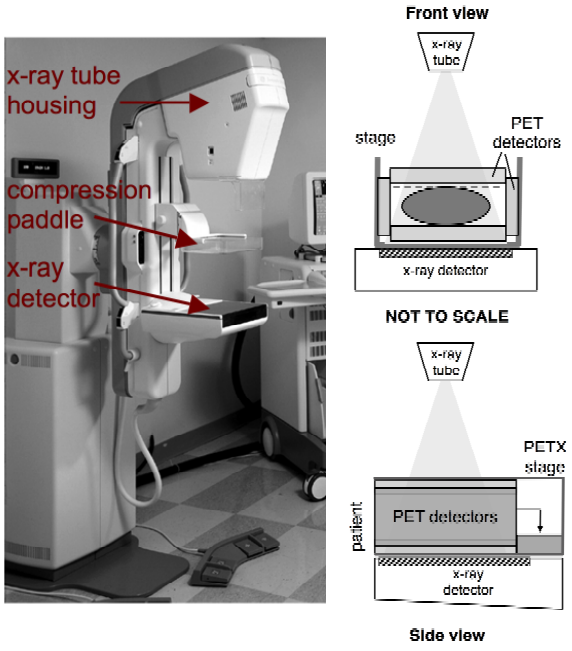

Fig. 1. PET/X concept: a four-sided PET scanner mounts to a conventional mammography gantry. LEFT: conventional mammography gantry main components are x-ray tube, compression paddle, and x-ray detector. PET detector, illustrated at RIGHT, attaches to the x-ray detector, and is removed to acquire an x-ray mammogram.

We are adopting the monolithic crystal detector module design following previous work in our lab [21]. Through the use of monolithic crystals we hope to measure DOI with maximum-likelihood event positioning methods, and maximize sensitivity by limiting inter-crystal reflectors. For the intended clinical applications we wish to focus on the quantification task (i.e. assessment and test/retest). A previous study [22] suggested that in choosing between spatial resolution and photon sensitivity, resolution was more important to the assessment task (quantitative accuracy), whereas sensitivity was more important to the detection task. With this in mind we will favor spatial resolution in the PET/X system design. We can do this by making the scintillation crystals arbitrarily thin, however, at some point the sensitivity will become “too low”. The aim of this work is to characterize the spatial resolution versus photon sensitivity relationship as a function of crystal thickness for the proposed system geometry.

Mounting a box-shaped detector onto a mammography gantry poses challenges. Ideally the box detector is positioned as close as possible to the patient, meaning variable detector positioning to accommodate different patient sizes. Doing so complicates the data normalization and the mechanical design. We investigated the performance losses of a system with fixed detector separation relative to an adjustable system by comparing the resolution-sensitivity tradeoff for these two situations. In all, we compared the resolution-sensitivity tradeoff as a function of the following parameters:

- detector crystal thickness
- LOR estimation method (with and without DOI information)
- source position within the field of view
- object thickness

- detector separation

Apart from considering the fixed-detector system, aspects of integrating the PET detectors with the mammography gantry are not discussed in this paper.

II. Materials and Methods

A. Detector and Source Geometry

We used the SimSET Monte Carlo software [23] to track annihilation photon pairs in the PET/X system depicted in Fig. 2. The system and simulation parameters are given in table 1. References to the system orientation in this paper assume that the larger main detectors are horizontal, and the smaller side detectors are vertical, as suggested in fig. 1. This orientation corresponds to a craniocaudal view in mammography. The PET/X system will mount to a mammography machine such that the lower main PET panel is fixed parallel to the x-ray detector, and rotates with the gantry to acquire alternate mammography views (e.g. medio-lateral oblique). We varied the scintillation crystal thickness on the main (t_M) and side (t_S) detectors independently. The scintillation material was lutetium oxyorthosilicate (LSO). Details of the photo-sensors were not considered, except for modeling spatial resolution as described later in this section. In the SimSET model the LSO crystals were single, monolithic crystals. Monolithic crystals of these large sizes are not possible, so the actual system will be assembled from subunits of monolithic crystal detectors. We anticipate using square monolithic subunits 3-5 cm on a side, and inter-crystal reflective material < 0.1 mm thick, yielding > 99% packing fraction. No correction for crystal packing fraction was made to the SimSET results.

The main detector separation, corresponding to breast compression thickness, was modeled as 4 cm and 8 cm, and two uniform breast phantoms of adipose tissue with the same 4 cm and 8 cm thicknesses were used. Lateral dimensions of the breast phantoms were 20 cm x 7.5 cm (fig. 2). These phantoms provided background (BG) activity and scatter medium. In addition, we simulated point sources embedded in the BG phantoms. Two different size point sources were simulated: an 'ideal' point (0.1 mm) and a 2 mm diameter sphere. The ideal point source was in air (no BG phantom), and positron range and annihilation photon non-colinearity were not modeled. The 2 mm source was in the BG phantom and positron range and photon non-colinearity modeling was used. Data were generated for each of these small sources placed near the center and corner of the FOV (Fig. 2 and table 1).

Simulations were run separately for the background (adipose tissue phantoms with uniform activity, 5×10^6 events) and point sources (> 100k events). The 2 mm diameter point source simulations had cold adipose tissue background. In this work background and point source data were analyzed separately.

Table 1: PET/X Simulation Parameters

Property	Value(s)	Remarks
Detector dimensions	**Main detectors** 15 cm anterior-posterior 20 cm lateral **Side detectors** 15 cm anterior-posterior 10 cm superior-inferior	Anatomical orientation refers to the case of horizontal main detectors and vertical side detectors (craniocaudal mammographic positioning as shown in fig. 1)
Main detector separation	8 cm, 4 cm	
Detector scintillation crystal (LSO) thicknesses	5, 10, 20, 40 mm	Main detector crystal thickness (t_M) and side detector crystal thickness (t_S) varied independently.
Background object (adipose tissue)	7.5 cm anterior-posterior 20 cm lateral	
Background object thicknesses	8 cm, 4 cm	
		Positron range and coincidence photon acolinearity modeled in simulation?
Point sources	‘Ideal’ point (0.1 mm) in air	No
	2 mm diameter sphere in the background object	Yes
Point source locations	**8 cm main detector separation:** center source (x,y,z) = (0, -5, -37.5) mm corner source (x,y,z) = (-80, -30, -37.5) mm **4 cm main detector separation:** center source (x,y,z) = (0, -5, -37.5) mm corner source (x,y,z) = (-90, -15, -37.5) mm	See fig. 2 for coordinate system.

PET/X simulation setup is illustrated in fig. 2.

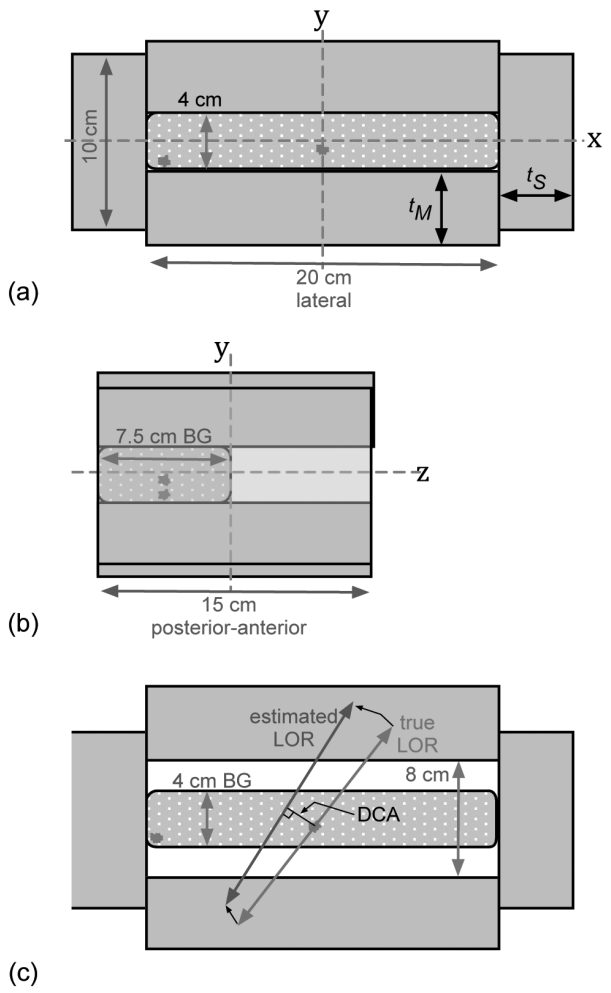

Fig. 2. (a) Front view (*x*-*y* plane) showing: main detectors separated by 4cm, a 4 cm thick background source, and two point-sources at (*x*,*y*)=(0, -0.5) and (-9, -1.5) cm. LSO crystal thickness are t_M and t_S (PMTs not shown). (b) Side view (*y*-*z* plane): point-sources are at *z* = -3.75 cm. Background source is 7.5cm thick in *z*. (c) Front view of system with main detectors now separated by 8cm with the same 4cm thick object. An 8cm thick object was also simulated for this configuration. Distance of closest approach (DCA) is the orthogonal distance between the estimated LOR and the center of the point source, as illustrated (distance between LORs is not to scale).

B. Data Modeling

We set the LSO thickness equal to 40 mm on both main and side detectors in the SimSET simulations. Data were stored in list-mode format, and then filtered to keep only interactions that occurred completely within the specific crystal thickness being investigated. We processed data for 5, 10, 20, and 40 mm thick crystals, including combinations whereby side detector thickness was different than main detector thickness. Absolute photon detection sensitivity was calculated as:

Sensitivity = (No. of detected coincidence pairs) / (No. of decays) (1)

Coincidence events between any two of the four detectors were kept. The number of interactions of each 511 keV photon within the scintillation crystal was recorded; consecutive individual interactions that occurred within the crystal thickness were kept as valid events. Individual interactions occurring outside the crystal thickness, and any subsequent interactions regardless of position, were rejected. Events where a single photon interacted in both a main and a side detector were rejected. An energy threshold of 400 keV was applied. Finite detector energy resolution was not modeled as we assumed this would have little impact on overall sensitivity and the effect of energy blurring on the positioning calculations was neglected. Scatter fraction (SF) was calculated as the ratio of recorded events depositing less than 400 keV to all recorded events. Random coincidence events were not simulated or estimated. The fractions of events with just one interaction (i.e. photo-electric), or 2-3 interactions, or >3 individual interactions were calculated as a function of crystal thickness.

We processed SimSET list-mode data to model the detection process in a position-sensitive scintillation crystal detector. Through this data modeling we estimated positions that would be measured for each photon pair, and from these positions coincidence lines of response (LORs) were estimated. The SimSET list-mode data consisted of 3-dimensional position coordinates and the deposited energy of each interaction. Event positions were estimated by modeling the detection process with and without DOI information. First, we estimated the lateral position of each photon with a two-dimensional center of mass calculation (2D-COM), weighted by energy, using the lateral coordinates of all interactions of an incident photon. The depth coordinate was assigned to a constant value equal to the average penetration depth of a normally incident 511 keV photon into the thickness of crystal under study. This case corresponds to no DOI information. To model finite detector spatial resolution,

we blurred the 2D-COM lateral position using a 2D Gaussian with symmetric 2 mm full width at half maximum (FWHM).

A second LOR estimation method was a 3D-COM based on the energy-weighted three-dimensional center of mass calculation of all three position coordinates. In this case the 2 mm FWHM 2D Gaussian was again applied to the lateral coordinates. We applied a DOI blurring based on DOI resolution measured previously in our lab [21] as summarized in table 2.

Table 2: Measured DOI resolution in monolithic crystals

Crystal thickness (mm)	DOI FWHM (mm)
1	1.0*
8	3.5
15	4.8

*DOI resolution of 1 mm for 1 mm thick crystal was assumed, not measured.

We used the measured data and assumed DOI resolution = 1mm for a 1mm thick crystal to obtain via least-squares fit (in mm):

$$\text{DOI FWHM} = (\text{crystal thickness})^{0.59} \quad (2)$$

The DOI coordinate of the 3D-COM position was blurred using a 1D Gaussian with FWHM given by (2). Blurred positions were recalculated if the blurring process placed an event outside of the crystal boundary so no events were lost due to blurring.

We also extracted the positions of the first interactions of each 511 keV photon to generate 'first-vertex' LORs as a gold standard. We analyzed the first-vertex LORs with and without applying the detector blurring described above.

We studied the relationship between the true point source LOR positions and three LOR estimates: LORs from (i) first-vertex data (with and without detector blurring), (ii) 2D-COM, and (iii) 3D-COM coordinates.

C. Event Mis-positioning: Distance of Closest Approach (DCA) and FWHM-distance (d_{FWHM})

We derived two event-positioning metrics to evaluate spatial blurring from the estimated LOR data. The first is the distance-of-closest-approach (DCA, Fig.2C); DCA is defined as the shortest (orthogonal) distance from the center of the point source to the LOR estimated from simulated interaction data. Each recorded coincidence event has an associated DCA that indicates the best positioning that could be accomplished with the given LOR estimation. Histograms of DCA values were generated for events detected from the various point sources. The DCA for ideal point sources should be zero (neglecting pixel discretization effects), and for the 2 mm point source the DCA values should be less than or equal to 1 mm. DCA values will deviate from the ideal due to multiple effects: incorrect DOI coordinate, finite detector resolution, multiple-interactions, low-angle scatter in the object (an energy threshold of 400 keV was applied to detected events), positron range, and non-colinearity.

The DCA metric is strictly positive with a skewed distribution, so the mean and standard deviation are not appropriate summary statistics. For example, infrequent events that result in large DCA may influence the mean DCA disproportionately relative to how such sparsely distributed events would influence spatial resolution. Using the median DCA mitigates this bias but we sought an additional metric that directly incorporated the distribution of DCA values as a volumetric event density. To this end, we considered the distribution given by the cumulative sum of events with DCA less than some distance from the source center. For the 0.1 mm point source in air the cumulative sum of events with DCA $\leq$ 0.1 mm would ideally be 100% (again, neglecting pixel discretization). For the 2 mm point source, summing the DCA distribution to a distance of 1 mm would include 100% of events in the case of no event mispositioning. In practice DCA values will be larger than the source radius due to physical blurring effects that cause DCA to deviate from the ideal. Next we considered a theoretical ideal point source whose position is blurred in three dimensions by an isotropic 3D-Gaussian distribution with standard deviation of σ. The normalized integral of this distribution over a sphere of diameter FWHM=2.35σ is 0.29:

$$\left(2\pi\sigma^2\right)^{-3/2}\int_0^{2\pi} d\phi \int_0^{\pi} \sin\theta\, d\theta \int_0^{fwhm/2} r^2\, dr \cdot \exp(-r^2/2\sigma^2) = 0.290 \quad (3)$$

The interpretation is that 29% of all events lie within one FWHM distance from the source center. We then defined a

spatial resolution metric called the FWHM-distance (d_{FWHM}) as the distance from the source center where the cumulative sum of DCA values equals 29% of the total number of detected events. The d_{FWHM} metric is analogous to the distribution median, except that the d_{FWHM} is defined as the distance that divides the DCA distribution into a 29%-71% split rather than a 50% - 50% split as defined by the median. Calculation of d_{FWHM} is illustrated in fig. 5.

As a reference for the relationship between the d_{FWHM} metric and system spatial resolution, we calculated the DCA and d_{FWHM} for line source data measured on a clinical PET/CT scanner (Discovery STE (GE Healthcare, Waukesha, WI)) and compared these metrics with the reconstructed spatial resolution of the line sources. The measured data used a set of 12 cm long line sources, 0.8 mm internal diameter, positioned at eight radial offset locations each separated by 3.5 cm [24]. The line sources were parallel to the scanner axis. Data were acquired in 3D-mode then reconstructed using Fourier rebinning and filtered back-projection. Line source FWHMs were calculated graphically by interpolation from image profiles using the method described in the NEMA Standards Publication NU 2-2001 Performance Measurements of Positron Emission Tomographs. We averaged spatial resolution across 6 axial slices (2 cm). In calculating DCA for the DSTE scanner, we assumed that the sinogram radial bin with the highest counts in each azimuthal view corresponded to the true point source position and a DCA value of zero. Finite DCA values were assigned to adjacent radial bins according to their spacing. This exercise was meant to illustrate the correlation between spatial resolution and the d_{FWHM} metric in support of our hypothesis that d_{FWHM} is a surrogate for spatial resolution.

We calculated sensitivity and d_{FWHM} for the PET/X simulated data as functions of detector crystal thickness. We then related sensitivity and d_{FWHM} via common crystal thicknesses and present the data as d_{FWHM} vs. sensitivity.

III. Results

A. Sensitivity, Scatter, and Multiple-interactions

Fig. 3 shows the absolute sensitivity, scatter fraction, and multiple-interactions fractions as a function of scintillator crystal thickness for the variety of scanner configurations under study. Data are presented as a function of the main detector crystal thickness. Two cases of side detector crystal thickness are included: side detector thickness equals main detector thickness, or side detector is fixed at 20 mm. The sensitivity vs. crystal thickness relationship of the centered 2 mm sphere source in background medium correlated very closely with the background sensitivity (R^2 = 1.0, slope = 0.94).

B. Distance of Closest Approach (DCA) and FWHM-distance (d_{FWHM})

Fig. 4 shows the distribution of DCA values for an ideal point source and a 2 mm sphere source from two different simulations. The ideal point source was simulated in air and positron range and non-colinearity were not modeled, whereas these effects were modeled for the 2 mm source that was in adipose scatter medium. Furthermore, for the data presented in fig. 4, detector resolution blurring was not applied to the ideal point source but was applied to the 2 mm source. Fig. 4 shows the case of 20 mm thick crystals on both side and main detectors.

Fig. 5 shows normalized cumulative sums of DCA histograms. These distributions determine d_{FWHM} values as illustrated.

Fig. 6 compares the DCA-based mispositioning metrics to reconstructed spatial resolution as a function of radial position in the whole-body PET scanner field of view. The average bias and RMS error between spatial resolution and d_{FWHM}, DCA-median, and DCA-mean are given in table 3.

Sensitivity of the background object and the centered 2 mm source were nearly equivalent as noted above in section III.A. Fig. 3B shows the relationship between point-source sensitivities in the center and corner of the FOV. In the

remainder of this section the reported sensitivities are those of the background objects.

In fig. 7 we compare the influence of DOI information and finite detector spatial resolution on the sensitivity versus mis-positioning tradeoff. To do this we use data from the ideal point source in air for which positron range and non-colinearity were not modeled in SimSET.

The effects of DOI information can be seen by comparing the 3D-COM and 2D-COM data in fig. 7. Additionally, we see the effects of multiple interactions by comparing the first-vertex data to the 3D-COM data. Incorporating finite detector spatial resolution reduces the difference in d_{FWHM} between the three LOR estimation methods, mainly by degrading d_{FWHM} of the first-vertex and 3D-COM data closer to values obtained with the 2D-COM method. Note also that for the centered source there is a difference between 2D-COM and 3D-COM d_{FWHM}. This is due to the box geometry of the PET/X system. On a ring PET system no such difference would be expected (except perhaps a very small difference due to multiple interaction blurring).

Fig. 7 data are for the idealized point source in air and equal crystal thicknesses on the main and side detectors. Next we consider the 2 mm source surrounded by a scattering medium of adipose tissue and cases where crystal thicknesses on the main and side detector vary independently.

Fig. 8 shows d_{FWHM} and photon sensitivity versus crystal thickness on the main (t_M) and side (t_S) detectors. Fig. 8 contains projections of this 4-dimensional relationship onto the t_S - d_{FWHM} plane. Open circle markers in fig. 8 represent the calculated data points at the 16 t_M - t_S combinations of 5, 10, 20, and 40 mm each. The surface contour represents an interpolation of the 16 calculated data points, and the color of the surface mesh represents photon sensitivity. Columns of markers are at constnat t_S, and for each column the lowest marker is t_M = 5 mm and the highest marker is t_M = 40 mm. The surface plots can be viewed in this projection view without loss of data visualization because d_{FWHM} increases monotonically with t_M.

Sensitivity and d_{FWHM} vary in a monotonic relationship, proportional to crystal thickness. Since selection of crystal thicknesses does not lend itself to simultaneous optimization of d_{FWHM} and sensitivity, we will focus on obtaining the smallest d_{FWHM} achievable for a given minimum target sensitivity. As a preliminary sensitivity target we use a 5%-10% range. This is based on having geometric sensitivity somewhat higher than typical whole-body PET scanners [25]. The thick black dashed lines on the contour mesh in fig. 8 indicate the target sensitivity range of 5%-10%.

Sensitivity and d_{FWHM} vary more slowly with side detector thickness than with main detector thickness, likely due to the smaller subtended solid angle. Indeed, d_{FWHM} is largely independent of t_S for $t_M \geq 10$ mm when the source is centered in the FOV. However, for the sources in the corner of the FOV there is on average 5% increase of d_{FWHM} per centimeter increase in t_S. Results of four t_M-t_S combinations from fig. 8 that are close to our target sensitivity are given in more detail in table 4.

When the object was 4 cm thick, and the main detector separation was also 4 cm, the d_{FWHM} values differed by only a few percent from the values obtained with the 8 cm object shown in table 4. The system sensitivity for the 4 cm object (4 cm detector separation) increased to 7.2%, 12.8%, 14.8%, 25.0% for the four t_M-t_S combinations in the respective ascending order listed in table 4.

C. Comparison of different main detector separations for a fixed object size

To investigate performance loss due to a system with fixed main detector separation we compared sensitivity and d_{FWHM} for the 2 mm point sources in the 4 cm thick object when the main detectors were separated by 4 cm and 8 cm. Fig. 9 shows that, in addition to the expected sensitivity loss for larger detector separation, there is also a slight degradation of d_{FWHM} for a given system sensitivity.

IV. Discussion

In this simulation study we used the FWHM-distance metric (d_{FWHM}) to characterize spatial resolution in an analysis of the tradeoff between system sensitivity and spatial resolution on a rectangular box PET detector geometry. The d_{FWHM} is an event positioning metric that captures fundamental detector physics processes that determine limits of accurate placement of coincidence events, and is independent of the image reconstruction algorithm. We chose this approach due to the well-known confounding aspects of estimating image resolution when non-linear iterative image reconstruction methods are used. In these cases resolution can be artificially enhanced when noise amplification in background sources is not also considered. Using analytical reconstruction methods (e.g. filtered back-projection) requires considerable effort (e.g. [26]) and is not a goal of the PET/X project so has not been pursued thus far. In fig. 6 we demonstrated very good agreement between the d_{FWHM} calculated from measured data on a conventional cylinder PET scanner and the corresponding measured system spatial resolution. The definition of d_{FWHM} should make it applicable to PET detectors of any geometry; verifying that d_{FWHM} reflects spatial resolution in PET/X will require comparing with measured data in the future. We note that d_{FWHM} captures the effects of several phenomena leading to positioning errors, including (a) parallax, (b) multi-hit interactions, (c) positron range and non-colinearity, (d) finite detector spatial resolution, and (e) small angle scattered events accepted by an energy threshold below 511 keV. Our simulations showed that d_{FWHM} approaches zero when effects (a)-(e) were removed (fig. 7, 1st-vertex with detector blur OFF). In future work we plan to correlate these metrics with reconstructed images and in particular with image quantitative accuracy.

We are evaluating the sensitivity-resolution tradeoff in the PET/X system in the context of the intended clinical application of assessment of radiotracer uptake in small (< 2 cm) lesions in the breast. We modeled our detector-object configuration based on a study of patients imaged with a positron emission mammography system [27], in which the mean detector separation was ~7.5 cm and the breast tissue filled roughly half of the 24 cm X 16.4 cm field of view of the scanner used in that work. Based on results in [22] we assume that spatial resolution is more important than sensitivity for achieving accurate image quantification. Put another way, we assume a certain level of spatial resolution is required (both FWHM and uniformity of FWHM within the FOV) to overcome parallax and partial volume effects and achieve clinical quantitative accuracy goals, even in an ideal case of noise-free data. Improving spatial resolution by reducing crystal thickness also reduces photon sensitivity, which can in turn degrade quantitative precision. Our approach was to examine the sensitivity-vs-resolution space for a range of crystal thicknesses where one metric changes relatively slowly while the other improves or degrades appreciably. We found this scenario in the case of increasing side detector thickness (t_S): our resolution metric (d_{FWHM}) degraded negligibly while sensitivity increased appreciably. In searching this space we remain cognizant that sensitivity cannot be arbitrarily reduced. We thus set a preliminary minimum sensitivity target of 5-10% based on typical whole-body PET scanner geometric sensitivity. By targeting this sensitivity we hope to use similar injected doses (~10 mCi) and acquisition times (~5 min.) as whole-body PET. Using extremely low doses is not the emphasis for the clinical application of assessing patients with confirmed cancer, unlike the case for screening or diagnostic imaging applications. On the other hand, using PET as a therapy biomarker can entail serial scans for which the lowest possible dose is desired. We focused on the results of the 8 cm thick object; by targeting sensitivity of ~7.5% for an 8 cm thick object we hope to maintain > 5% sensitivity for larger breasts that may require 10-15 cm detector separation.

The proximity of the breast to the PET/X detectors allows us to achieve our target sensitivity with significantly thinner scintillation crystals than in whole-body PET. This simulation study suggested that we could achieve roughly the same geometric sensitivity as a whole-body PET scanner

(~5-10%) while using 10 mm thick crystals. It should be noted that sensitivity will vary with separation of the larger main detector panels.

By taking advantage of the fact that parallax errors are smaller on the side-detectors in the rectangular box geometry, we may be able to substantially increase system sensitivity with minimal resolution degradation by increasing just the side-detector crystal thickness. Indeed, fig. 8 shows little change of d_{FWHM} with side crystal thickness for the source in the center of the FOV. The d_{FWHM} did increase with side crystal thickness for the corner source, on average by 4% (8%) per centimeter increase in side crystal thickness with (without) DOI information. In this study the corner sources are in extreme corners of the FOV. In the proposed PET/X system we may be able to prevent positioning lesions in such extreme corners by using the mammography gantry rotation to selectively position lesions of interest closer to the center of the scanner FOV. Thus, while our results show that increasing the side detectors thickness leads to degradation of d_{FWHM} for corner sources, the effect may be minimal in the practice because of our ability to position lesions of interest away from extreme corners of the FOV.

The relative benefit of measuring DOI decreases with decreased crystal thickness. Our results show that, for crystal thicknesses of 10 mm on the main detector, and either 10 or 20 mm on the side detectors, spatial resolution (d_{FWHM}) for the central source was ~15% worse without DOI, and ~20-25% worse for the corner source (table 4). We must evaluate the benefits of adding DOI capability to the PET/X system against the associated cost and complexity, again in the context of the intended clinical application. One limitation to the present analysis is the use of a fixed 2 mm FWHM resolution in the lateral dimensions of the detectors. In practice the lateral resolution also improves in thinner crystals [21]. Thicker crystals will suffer more of a resolution penalty than reported here due to this simplification. The next step in this work is to develop image reconstruction models in order to determine how the data-based metrics investigated in this study relate to image-based metrics, particularly to quantitative accuracy.

Designing PET/X with fixed detector positions, as opposed to a system that adjusts to be as close to the patient as possible, would greatly simplify data corrections (normalization) and the mechanical framework. We found that in addition to lower sensitivity for larger detector spacing, the d_{FWHM} of the corner source was increased (fig. 9B). This latter effect may not be observed in practice given the arguments made above about positioning lesions away from extreme corners in the PET/X FOV.

This study had several limitations, including not modeling the effect of random coincidences and activity outside the field of view. There were several reasons for this. First was that we are primarily interested in the impact of true and scattered coincidences arising from activity solely inside the field of view as these will determine the 'signal' i.e. resolution, whereas random coincidences and activity outside the field of view will primarily effect noise (under the reasonable assumption that the bias can be accurately estimated). Efforts to optimize injected dose and acquisition time are beyond the scope of the present work, which does not include estimates of random coincidence events, activity outside the field of view, or system dead-time characteristics that are needed to estimate noise equivalent count rates and other parameters related to absolute activity levels.

Scatter fraction and the fraction of multi-hit interactions were calculated to observe relative comparisons between phantoms and detector configurations simulated here. The effects of scatter and multi-hit fractions relevant to this work are captured by the spatial resolution metrics. Scatter fraction is also important for noise equivalent count calculations that will be studied in future work.

V. Conclusion

Our results showed that for the rectangular box PET system simulated here, increasing crystal thickness on the smaller side detectors provides a significant boost to system sensitivity with negligible loss of spatial resolution in the FOV center. In an extreme corner of the FOV resolution loss was ~5% per centimeter of increased side detector crystal thickness. Spatial resolution was 15%-25% worse without

using DOI information for the target crystal thicknesses of 10-20 mm. These findings suggest we can use thicker crystals on the side detectors and DOI measurement may not be needed on the PET/X scanner.

ACKNOWLEDGMENT

We thank David Mankoff, Hannah Linden, Robert Harrison, Tom Lewellen, Adam Alessio, and Larry Pierce for very helpful discussions and data related to this project.

REFERENCES

[1] Linden HM, Stekhova SA, Link JM, et al.: Quantitative Fluoroestradiol Positron Emission Tomography Imaging Predicts Response to Endocrine Treatment. J Clin Oncol 24(18):2793-99, 2006.

[2] Mankoff DA, Dunnwald LK: Changes in glucose metabolism and blood flow following chemotherapy for breast cancer. PET Clin 1:71-81, 2006.

[3] Dehdashti F, Mortimer JE, Trinkaus K, et al., PET-based estradiol challenge as a predictive biomarker of response to endocrine therapy in women with estrogen-receptor-positive breast cancer, Breast Cancer Res Treat 113:509-517, 2009.

[4] Kenny L, Coombes RC, Vigushin DM, Al-Nahhas A, Shousha S, Aboagye EO. Imaging early changes in proliferation at 1 week post chemotherapy: a pilot study in breast cancer patients with 3'-deoxy-3'-[18F]fluorothymidine positron emission tomography. Eur J Nucl Med Mol Imaging 2007;34(9):1339-47.

[5] Avril N, Rose CA, Schelling M, Dose J, Kuhn W, Bense S, Weber W, Ziegler S, Graeff H, Schwaiger M, Breast imaging with positron emission tomography and fluorine-18 fluorodeoxyglucose: use and limitations, J.Clin.Oncol., 18(20):3495-3502, 2000.

[6] Weber W: Use of PET for monitoring cancer therapy and for predicting outcome. J Nucl Med 46(6):983-995, 2005.

[7] Altekruse SF, Kosary CL, Krapcho M, Neyman N, Aminou R, Waldron W, Ruhl J, Howlader N, Tatalovich Z, Cho H, Mariotto A, Eisner MP, Lewis DR, Cronin K, Chen HS, Feuer EJ, Stinchcomb DG, Edwards BK (eds). SEER Cancer Statistics Review, 1975-2007, National Cancer Institute. Bethesda, MD, http://seer.cancer.gov/csr/1975_2007/, based on November 2009 SEER data submission, posted to the SEER web site, 2010.

[8] Thompson CJ, Murthy K, Weinberg IN, Mako F: Feasibility of positron emission mammography. Med Phys 21:529-538, 1994.

[9] Weinberg IN, Majewski S, Wojcik R, Weisenberger AG, et al.: Preliminary results for positron emission mammography: real-time functional breast imaging in a conventional mammographic gantry. Eur J Nucl Med 23:804-806, 1996.

[10] Turkington TG, Majewski S, Weisenberger AG, et al.: A large field of view positron emission mammography imager. IEEE NSS/MIC Conf. Record Vol 3, pgs:1883 – 1886, 2002.

[11] Wang GC, Huber JS, Moses WW, Qi J, Choong WS: Characterization of the LBNL PEM Camera. IEEE TNS 53(3):1129-1135, 2006.

[12] Abreu MC, Aguiar D, Albuquerque E, et al.: Clear-PEM: A PET imaging system dedicated to breast cancer research, Nucl Instr Meth A 571:81-84, 2007.

[13] R Raylman, S Majewski, M Smith, et al., The positron emission mammography/tomography breast imaging and biopsy system (PEM/PET): design, construction and phantom-based measurements, Phys Med Biol 53(3):637-653, 2008.

[14] SL Bowen, Y Wu, AJ Chaudhari, et al., Initial characterization of a dedicated breast PET/CT scanner during human imaging, J. Nucl. Med. 50:1401-08, 2009.

[15] LR MacDonald, J Edwards, T Lewellen, et al., Clinical imaging characteristics of the positron emission mammography camera: PET Flex Solo II, J Nucl. Med. 50:1666-1675, 2009.

[16] Ravindranath B, Junnarkar SS, Purschke ML, et al., Results from prototype II of the BNL simultaneous PET-MRI dedicated breast scanner, IEEE NSS/MIC Conference Record, pages 3315 – 3317, 2009.

[17] Furuta M, Kitamura K, Ohi J, et al., Basic evaluation of a C-shaped breast PET scanner, IEEE NSS/MIC Conference Record, pages 2548-2552, 2009.

[18] Iima M, Nakamoto Y, Kanao S, et al., Clinical performance of 2 dedicated PET scanners for breast imaging: initial evaluation, J. Nucl. Med. 53(10):1534-1542, 2012.

[19] Peng H, Levin C, Design study of a high-resolution breast-dedicated PET system built from cadmium zinc telluride detectors, Phys Med Biol, 55:2761-2788, 2010.

[20] Qi J, Kuo C, Huesman RH, Klein GJ, Moses WW, Reutter BW, Comparison of rectangular and dual-planar emission mammography scanners. IEEE Trans. Nucl. Sci. 49(5): 2089-96, 2002.

[21] Miyaoka RS, Li X, Hunter W, Pierce L, McDougald W, Kinahan P, Lewellen TK, Resolution Properties of a Prototype Continuous Miniature Crystal Element (cMiCE) Scanner, IEEE TNS, in press 2011.

[22] Lee K, Kinahan PE, Miyaoka RS, Kim JS, Lewellen TK. Impact of system design parameters on image figures of merit for a mouse PET scanner. IEEE Transactions on Nuclear Science 51(1):27-33, 2004

[23] Lewellen et al. The SimSET Program in Monte Carlo Calculations in Nuclear Medicine ed Ljungberg, Strand King (Phil, PA: Inst Phys Publ) pp 77–92, 1998.

[24] Alessio AM, Stearns CW, Tong S, et al., Application and evaluation of a measured spatially variant system model for PET image reconstruction, IEEE TMI 29(3):938:949, 2010.

[25] Cherry SR, Sorenson JA, Phelps ME, Physics in Nuclear Medicine, third edition, Saunders, 2003.

[26] Champley K, Raylman R, Kinahan P, Advancements to the planogram frequency-distance rebinning algorithm, Inv. Problems, 26 (2010) 045008.

[27] Wang CL, MacDonald LR, Rogers J, Avarakin S, Haseley D, Beatty D, Correlation of estrogen, progesterone, and her2neu receptor status and 18-F fluorodeoxyglucose and positron emission mammography, Am J Roentgenology, 197(2):W247-W255, 2011.

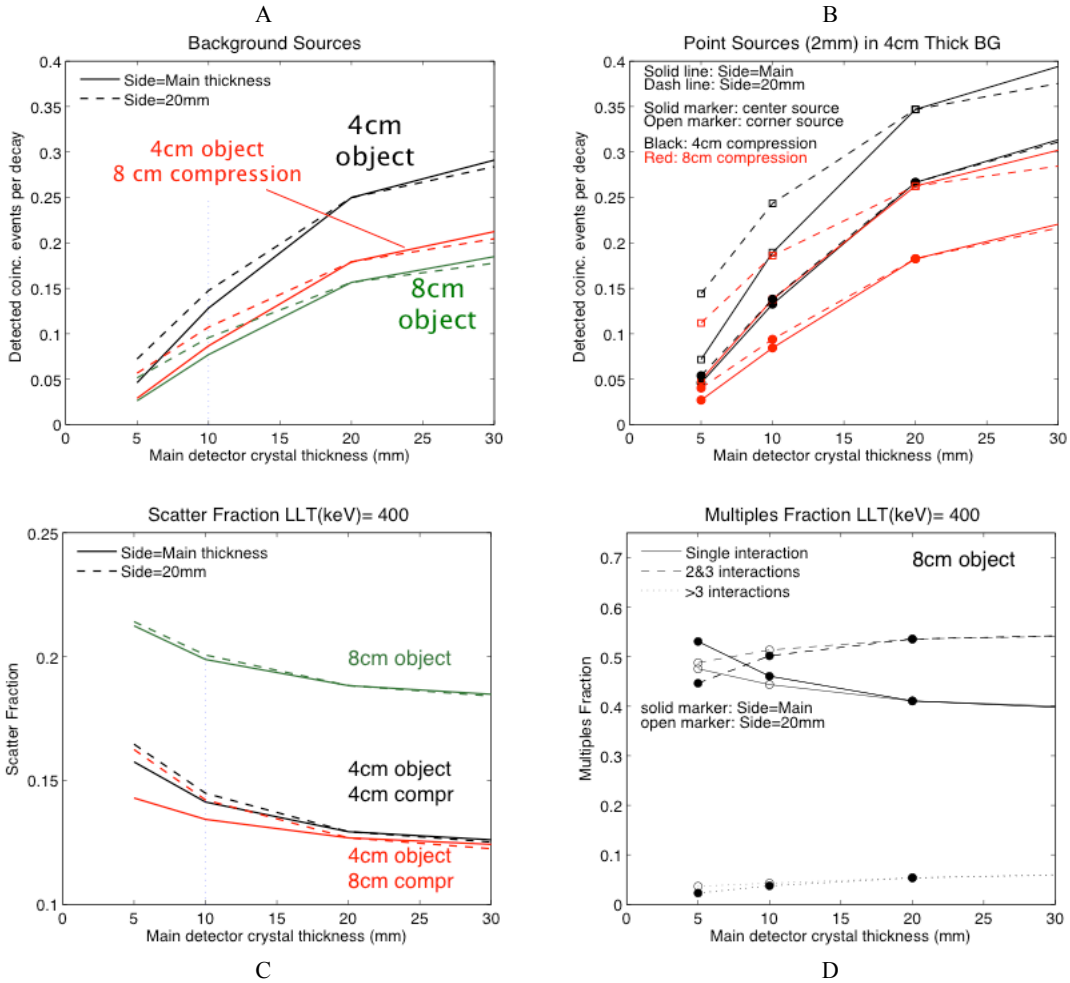

Fig. 3. (A) Coincidence sensitivity for the background sources (4 cm and 8 cm thick); 4 cm object-8cm compression corresponds to the arrangement shown in Fig. 2(C); phantom thickness and detector separation are equal in the other cases. (B) Coincidence sensitivity for the 2 mm diameter sphere sources in a 4 cm thick background (BG) phantom (Fig.2). (C) Scatter fraction. (D) Multiples fractions. In each plot data are shown for the case where the side detector crystal thickness is equal to the main detector crystal thickness, and where the side detector crystal thickness is fixed at 20mm while the main detector crystal thickness varies. The lower level threshold (LLT) on energy was 400 keV for all data.

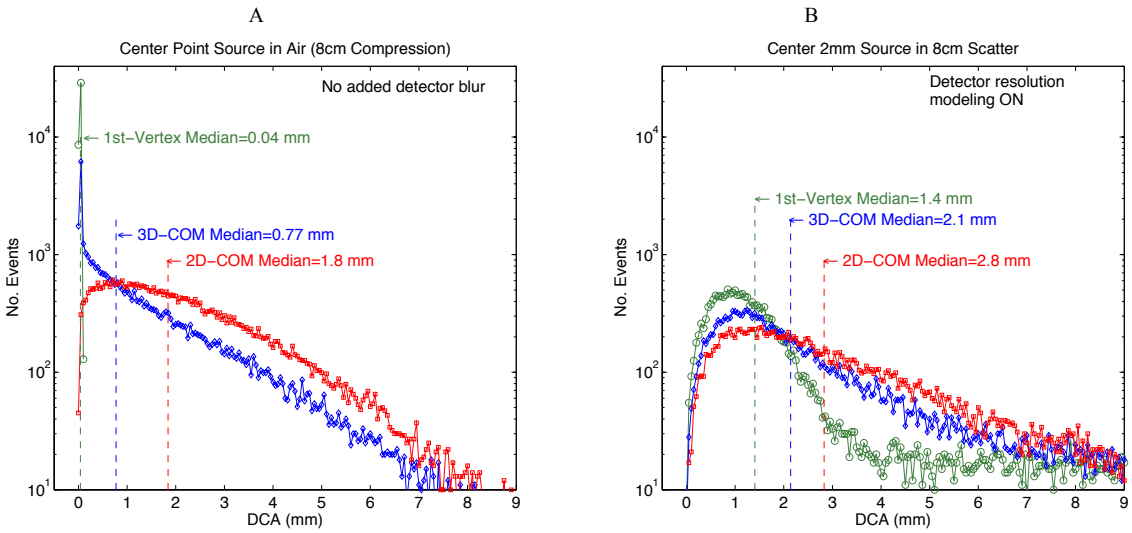

Fig. 4. DCA histograms for (A) point-sources in air, and (B) 2 mm diameter sphere source in the 8 cm thick adipose phantom. In (A) the detector resolution blurring was not used; LORs were estimated from the first-vertex, 2D-COM or 3D-COM calculations without further blurring. In (B) the detector blurring techniques were applied to all three LOR estimation methods, including the first-vertex. In both cases crystal thickness was 20 mm.

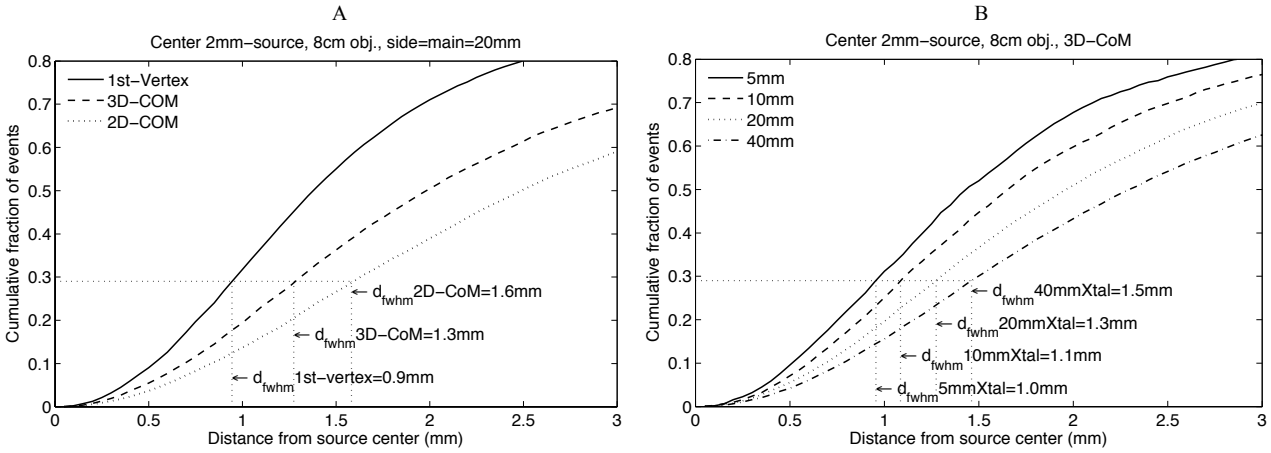

Fig. 5. Cumulative fraction of events with DCA less than the distance from the center of the 2 mm diameter source in 8 cm thick adipose background with detector resolution blurring applied. (A) Different LOR estimation methods at crystal thickness of 20 mm on main and side detectors; (B) different crystal thicknesses (main = side), LORs derived from 3D-COM. Determination of d_{FWHM} is illustrated for each curve.

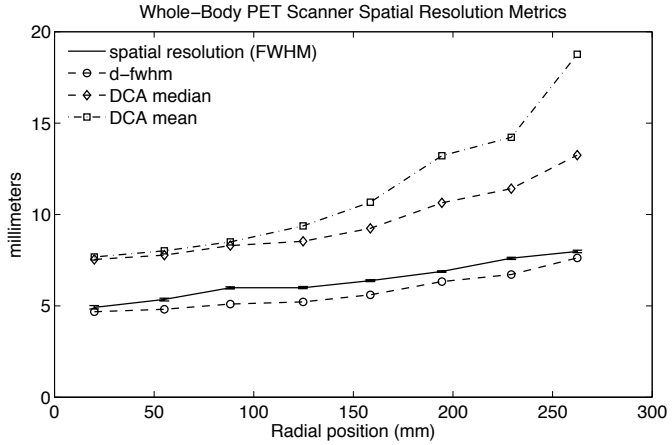

Fig. 6. Comparison of the system FWHM spatial resolution and DCA metrics measured on a whole-body PET scanner. Spatial resolution was averaged across six axial slices and the error bars correspond to ± one standard deviation.

Table 3: Correlation between DCA metrics and spatial resolution measured on a clinical PET scanner

DCA-metric	mean bias ± std. dev. (mm)	RMS error (mm)
d_{FWHM}	-0.63 ± 0.24	0.67
DCA median	3.20 ± 1.02	3.3
DCA mean	4.92 ± 2.87	5.6

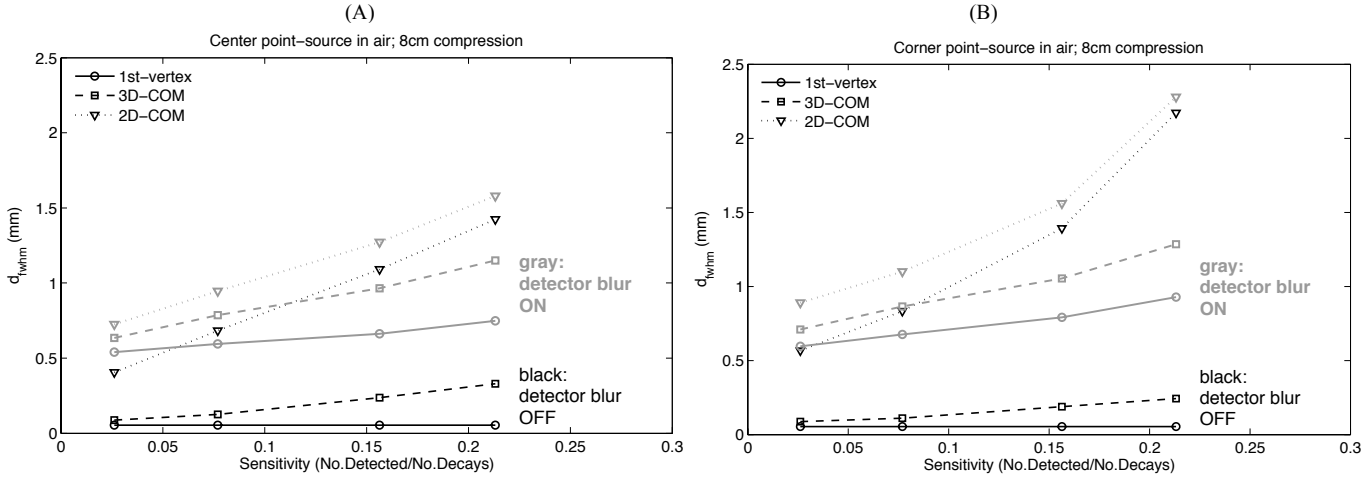

Fig. 7. Plot of d_{FWHM} vs absolute photon detection sensitivity for the ideal point source in air at (A) the FOV center, and (B) FOV corner. The four marker symbols on each curve correspond to crystal thicknesses of 5, 10, 20, and 40 mm (equal main and side detector thickness). Results are shown with and without applying detector spatial resolution blurring for all three LOR estimation methods.

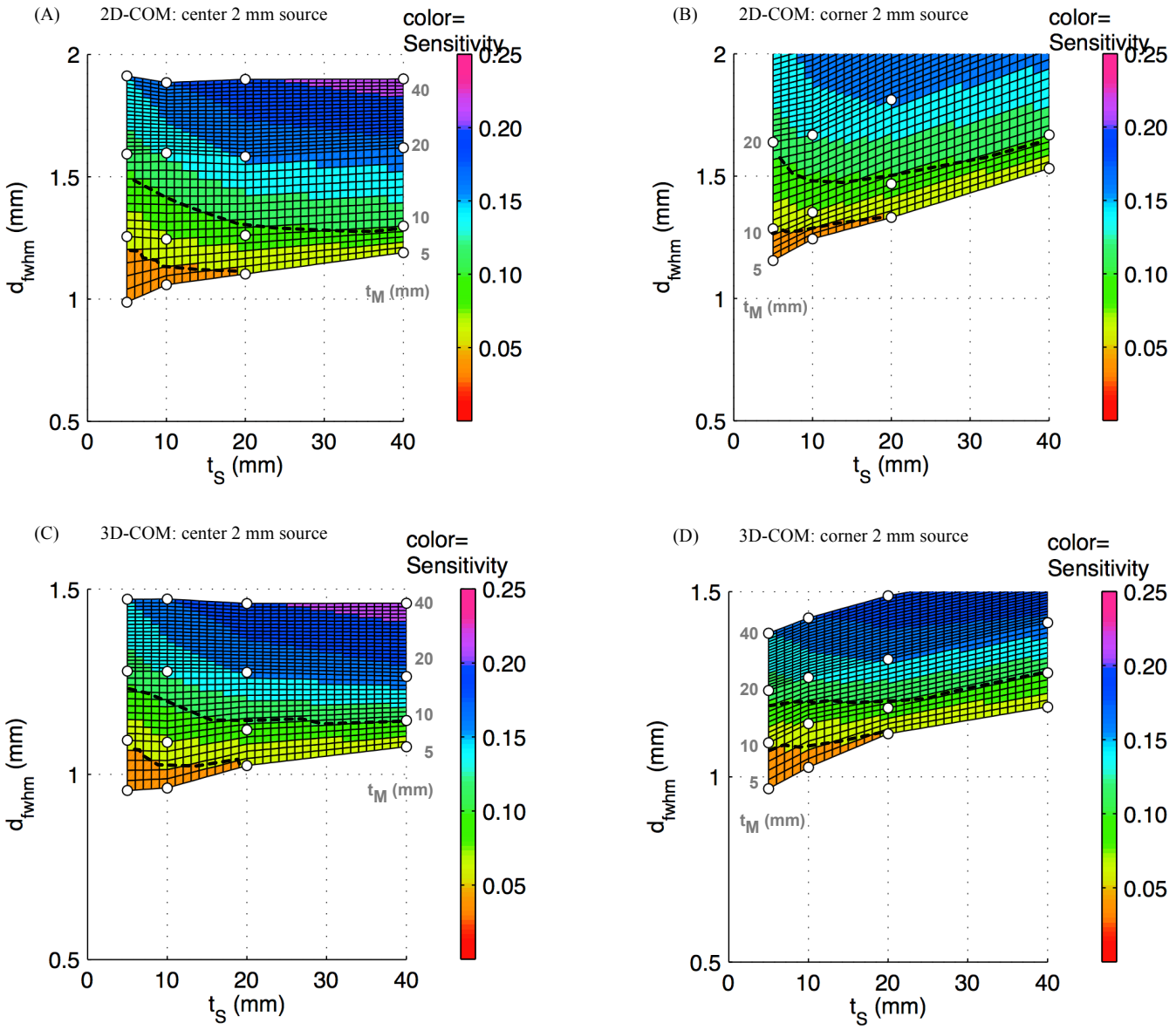

Fig. 8. Plots of d_{FWHM} and absolute photon sensitivity versus crystal thicknesses on the side (t_S) and main (t_M) PET/X detectors. These plots show data projected to the t_S - d_{FWHM} plane. The mesh surface represents an interpolation of the simulated data points that are shown by the circle markers. The four simulated t_M values (5, 10, 20, 40 mm) are found in the 'rows' of circle markers. Object thickness is 8 cm and detector spatial resolution blurring was applied in all cases. Results shown here are for the 2 mm diameter source: 2D-COM LOR estimator in (A) and (B); 3D-COM results in (C) and (D). Data from the center sources are in (A) and (C); from the corner sources are in (B) and (D). The black dashed curves follow the 5% and 10% sensitivity contours indicating our preliminary system sensitivity target range.

TABLE IV. SENSITIVITY AND 2D-COM VS 3D-COM d_{FWHM} AT SELECTED CRYSTAL THICKNESSES, 8 CM OBJECT

Crystal thickness	Background source Sensitivity	Center 2 mm source		Corner 2 mm source		
		2D-d_{FWHM}	3D-d_{FWHM}	2D-d_{FWHM}	3D-d_{FWHM}	
Main = 5 mm Side = 20 mm	5.2%	1.10 mm	1.02 mm	1.33 mm	1.12 mm	Absolute
		1.08	1.00	1.30	1.10	Relative[a]
Main = 10 mm Side = 10 mm	7.7%	1.24 mm	1.09 mm	1.35 mm	1.14 mm	Absolute
		1.22	1.07	1.32	1.12	Relative[a]
Main = 10 mm Side = 20 mm	9.6%	1.26 mm	1.12 mm	1.47 mm	1.19 mm	Absolute
		1.24	1.10	1.44	1.17	Relative[a]
Main = 20 mm Side = 20 mm	15.6%	1.58 mm	1.28 mm	1.81 mm	1.32 mm	Absolute
		1.55	1.25	1.77	1.29	Relative[a]

[a]Relative d_{FWHM} are normalized to the minimum d_{FWHM} in this table

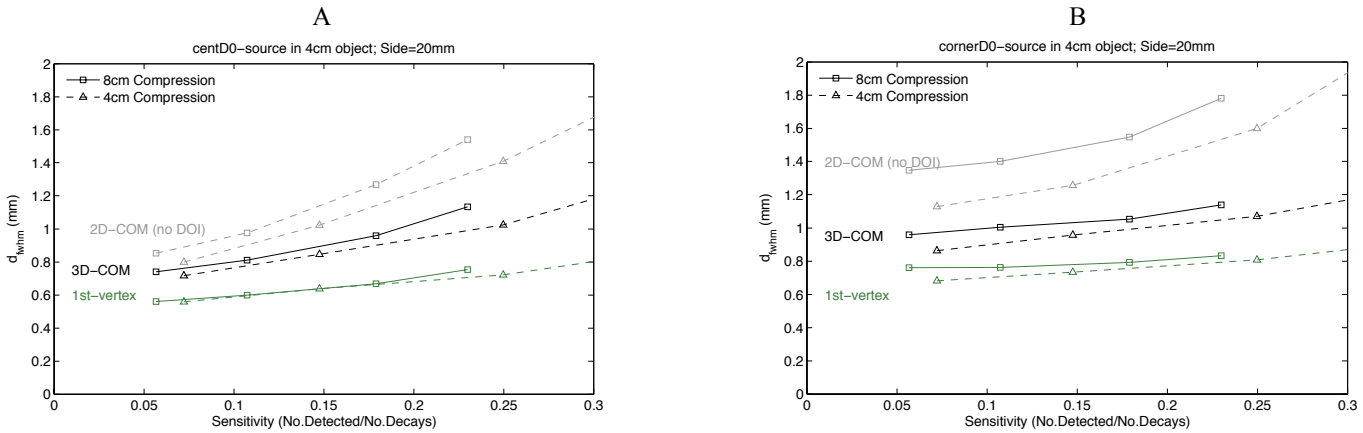

Fig. 9. Comparison of sensitivity and d_{FWHM} for the 2 mm source in the 4 cm thick object when the main detector separation is equal to the object thickness, or at a fixed larger separation of 8cm. (A) Center source. (B) Corner source. Marker symbols correspond to main detector thicknesses of 5, 10, 20, and 40 mm. Side detector thickness is fixed at 20 mm.

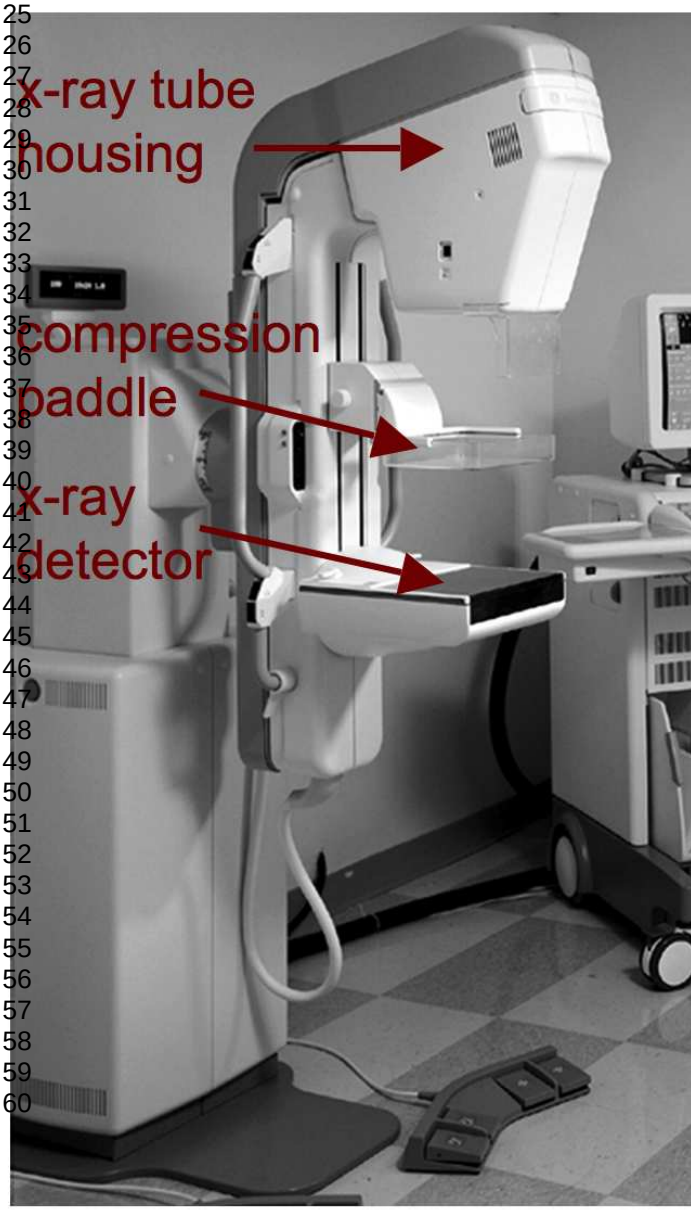
x-ray tube housing
compression paddle
x-ray detector

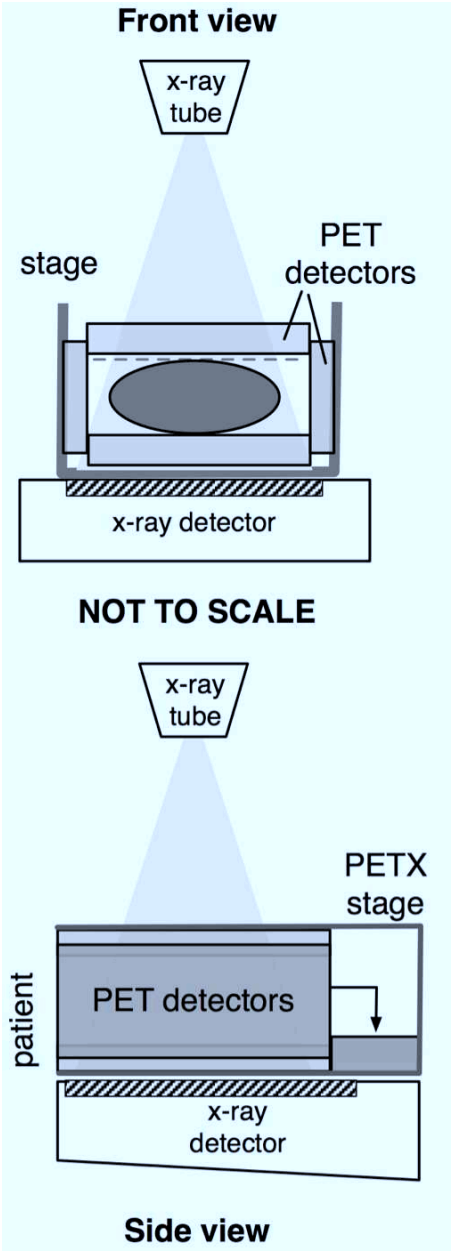
Front view
x-ray tube
stage
PET detectors
x-ray detector
NOT TO SCALE
x-ray tube
PETX stage
patient
PET detectors
x-ray detector
Side view

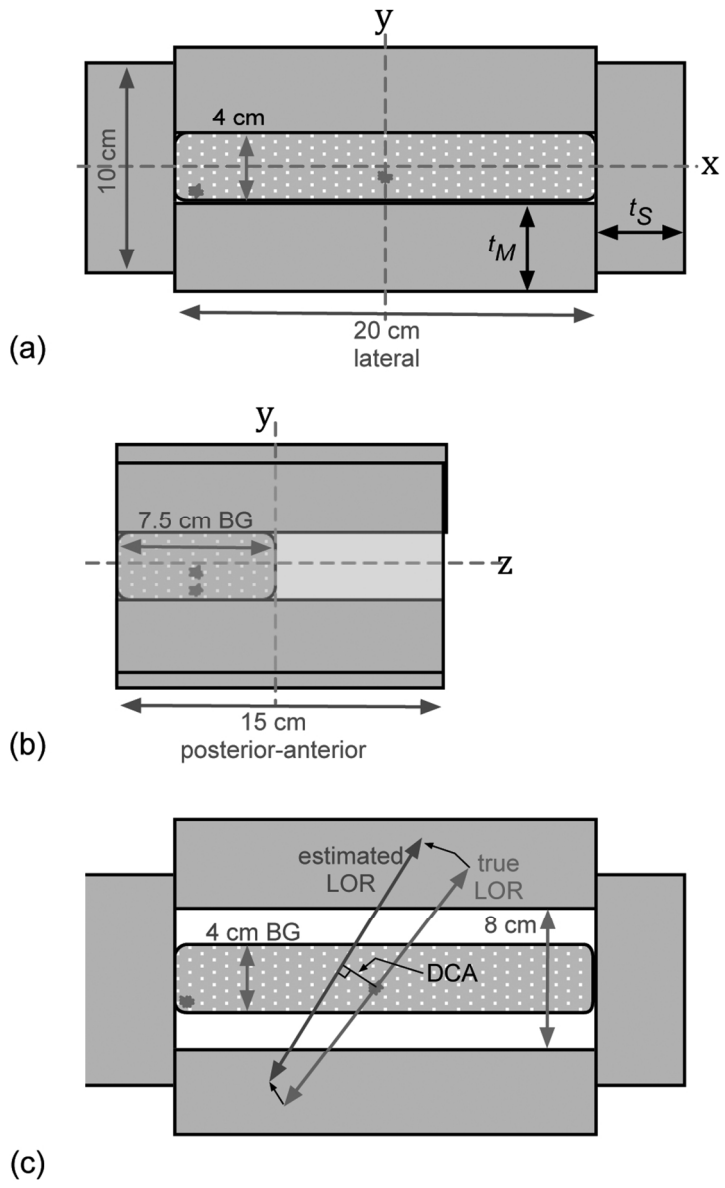

Fig. 2. (a) Front view (x-y plane) showing: main detectors separated by 4cm, a 4 cm thick background source, and two point-sources at (x,y)=(0, -0.5) and (-9, -1.5) cm. LSO crystal thickness are tM and tS (PMTs not shown). (b) Side view (y-z plane): point-sources are at z = -3.75 cm. Background source is 7.5cm thick in z. (c) Front view of system with main detectors now separated by 8cm with the same 4cm thick object. An 8cm thick object was also simulated for this configuration. Distance of closest approach (DCA) is the orthogonal distance between the estimated LOR and the center of the point source, as illustrated (distance between LORs is not to scale).
91x138mm (300 x 300 DPI)

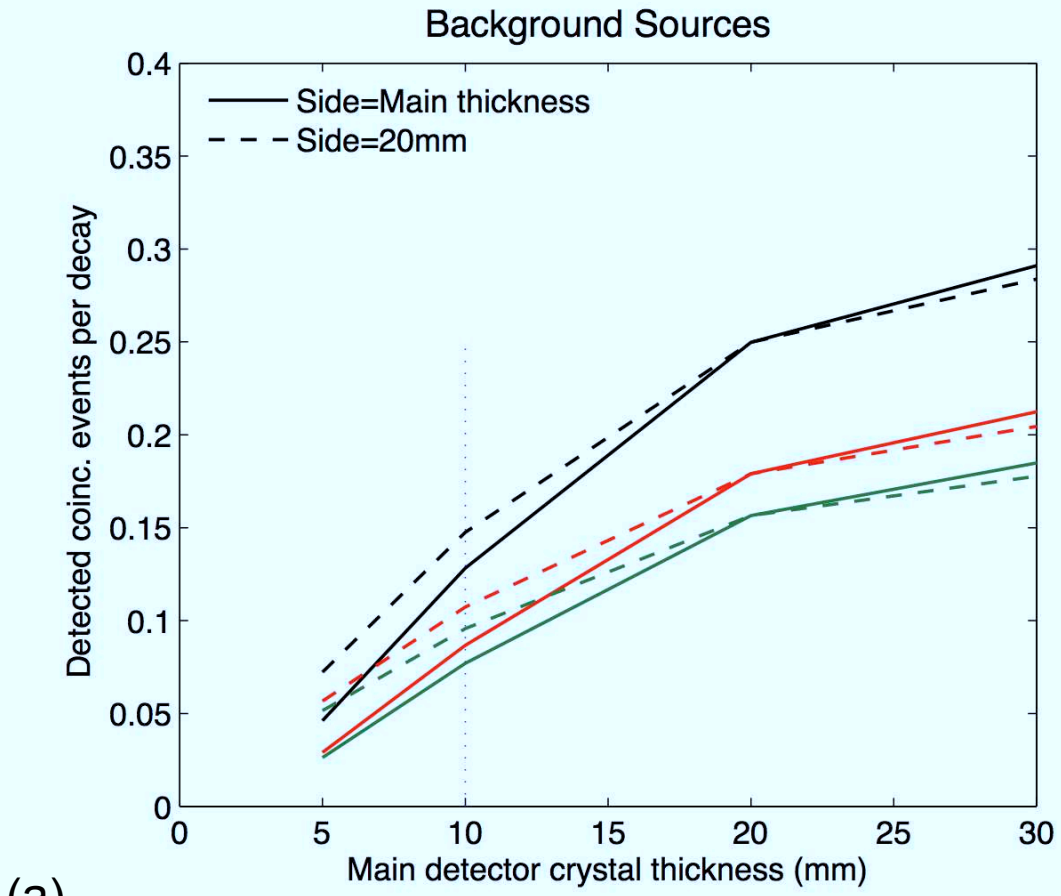
Background Sources
Side=Main thickness
Side=20mm
Detected coinc. events per decay
Main detector crystal thickness (mm)
0
0.05
0.1
0.15
0.2
0.25
0.3
0.35
0.4
0
5
10
15
20
25
30

(a)

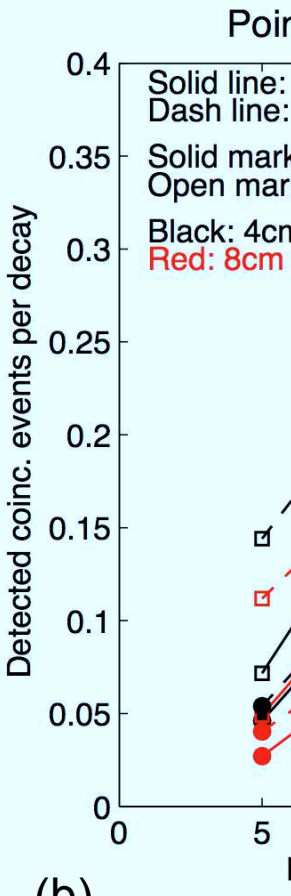
Poir
Solid line:
Dash line:
Solid mark
Open mar
Black: 4cm
Red: 8cm
Detected coinc. events per decay
0
0.05
0.1
0.15
0.2
0.25
0.3
0.35
0.4
0
5

(b)

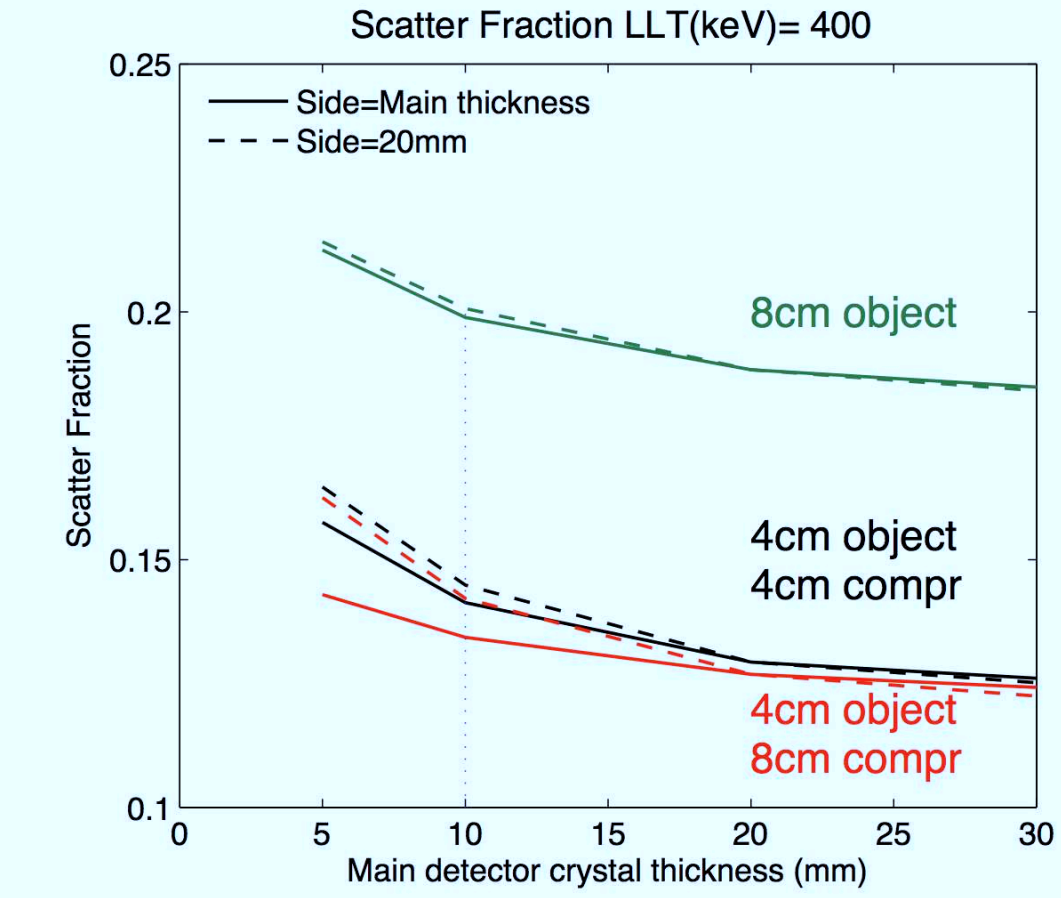
Scatter Fraction LLT(keV)= 400
Side=Main thickness
Side=20mm
8cm object
4cm object
4cm compr
4cm object
8cm compr
Scatter Fraction
Main detector crystal thickness (mm)
0.1
0.15
0.2
0.25
0
5
10
15
20
25
30

(c)

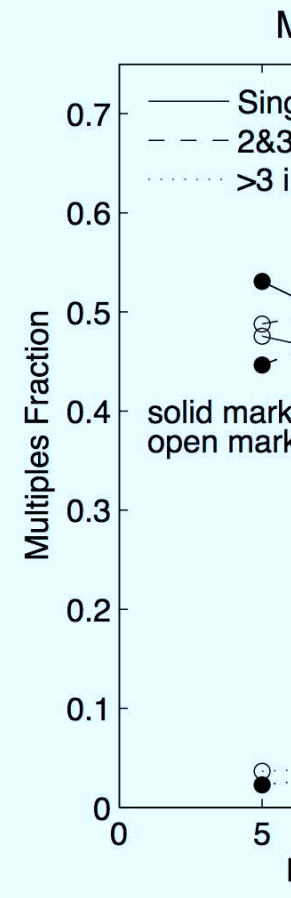
M
Sing
2&3
>3 i
solid mark
open mark
Multiples Fraction
0
0.1
0.2
0.3
0.4
0.5
0.6
0.7
0
5

(d)

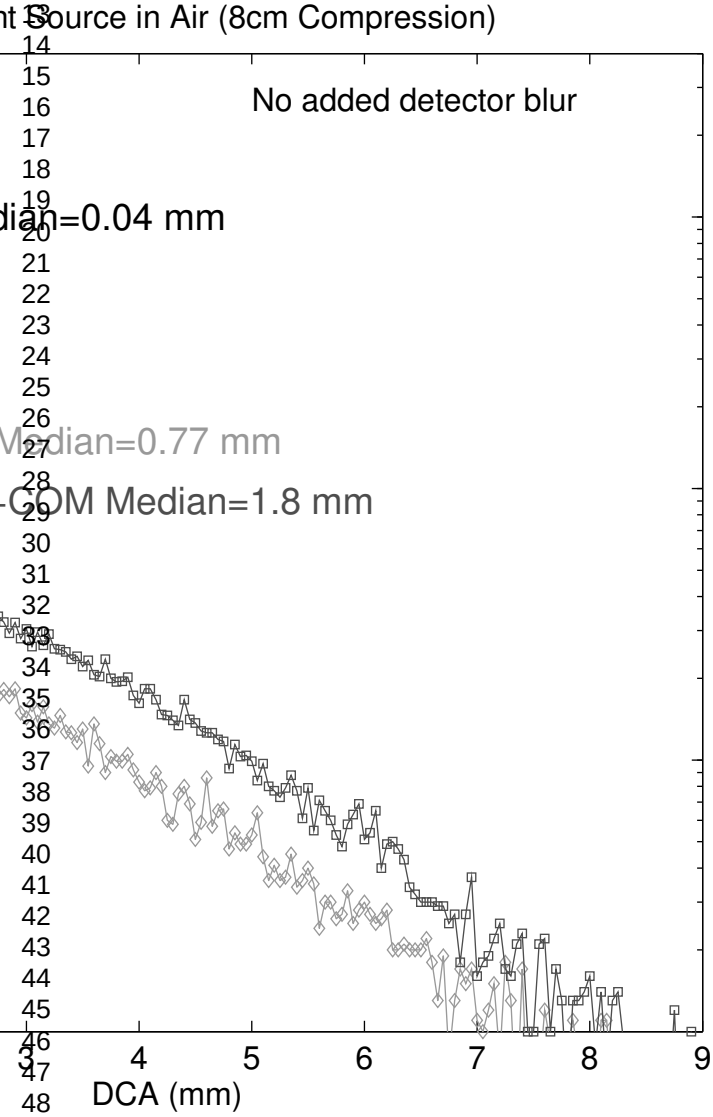
nt Source in Air (8cm Compression)
No added detector blur
dian=0.04 mm
Median=0.77 mm
-COM Median=1.8 mm
3
4
5
6
7
8
9
DCA (mm)

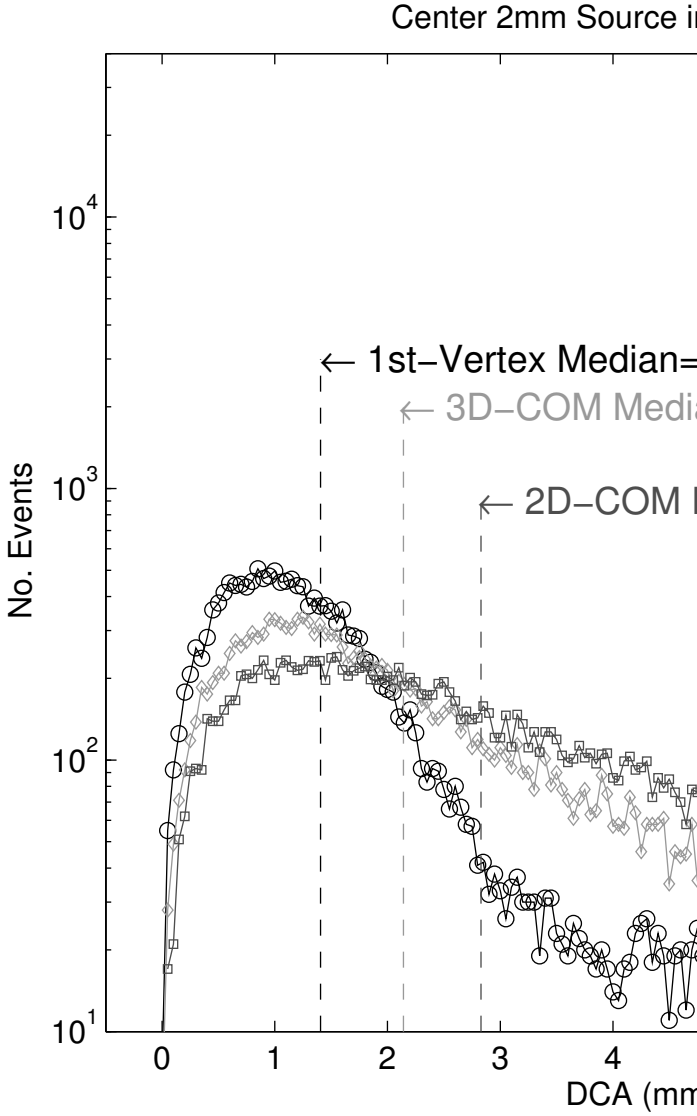
Center 2mm Source i
10^4
10^3
10^2
10^1
No. Events
← 1st−Vertex Median=
← 3D−COM Medi
← 2D−COM
0
1
2
3
4
DCA (mm

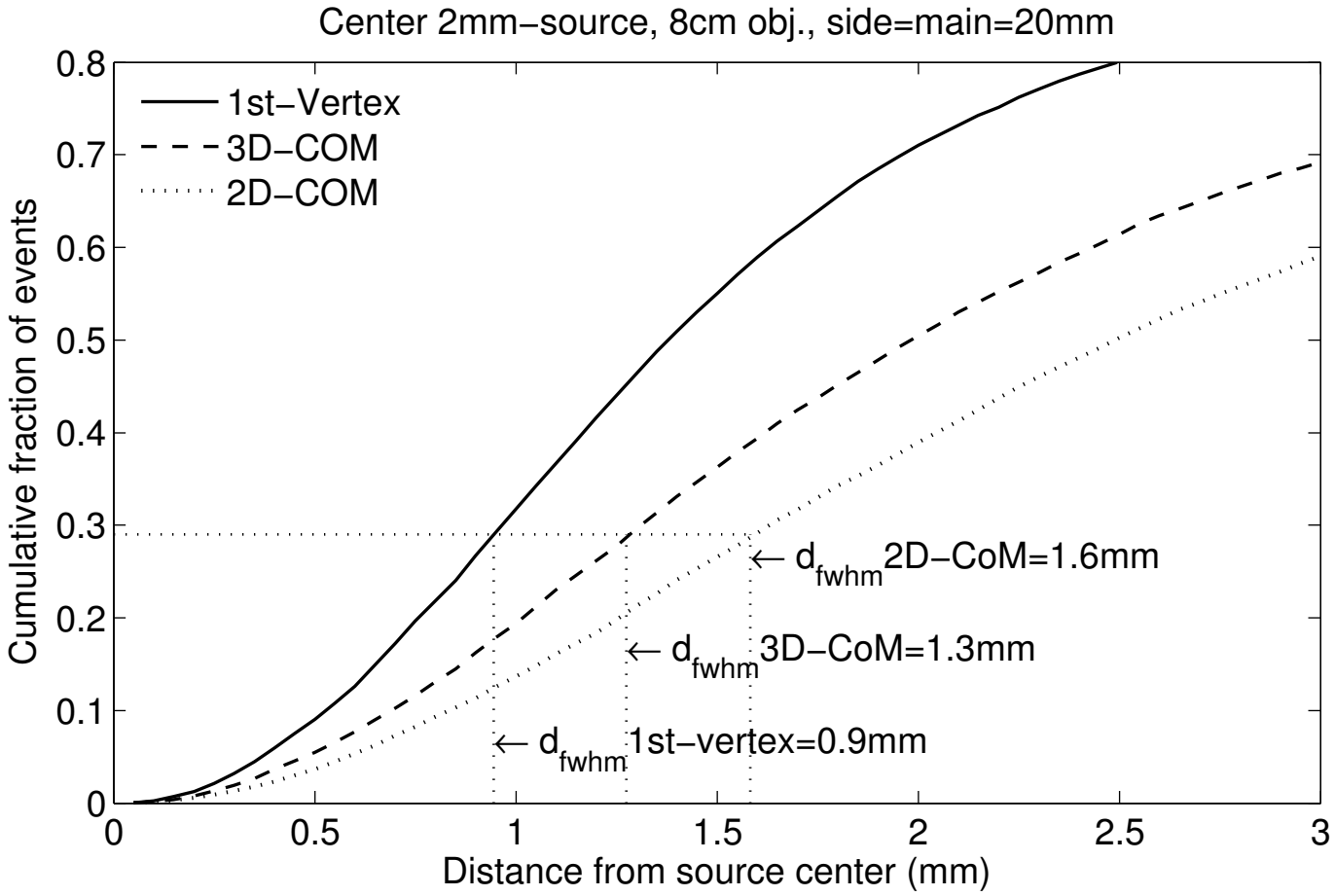
Center 2mm−source, 8cm obj., side=main=20mm
1st−Vertex
3D−COM
2D−COM
Cumulative fraction of events
Distance from source center (mm)
← d_fwhm 2D−CoM=1.6mm
← d_fwhm 3D−CoM=1.3mm
← d_fwhm 1st−vertex=0.9mm
0
0.1
0.2
0.3
0.4
0.5
0.6
0.7
0.8
0
0.5
1
1.5
2
2.5
3

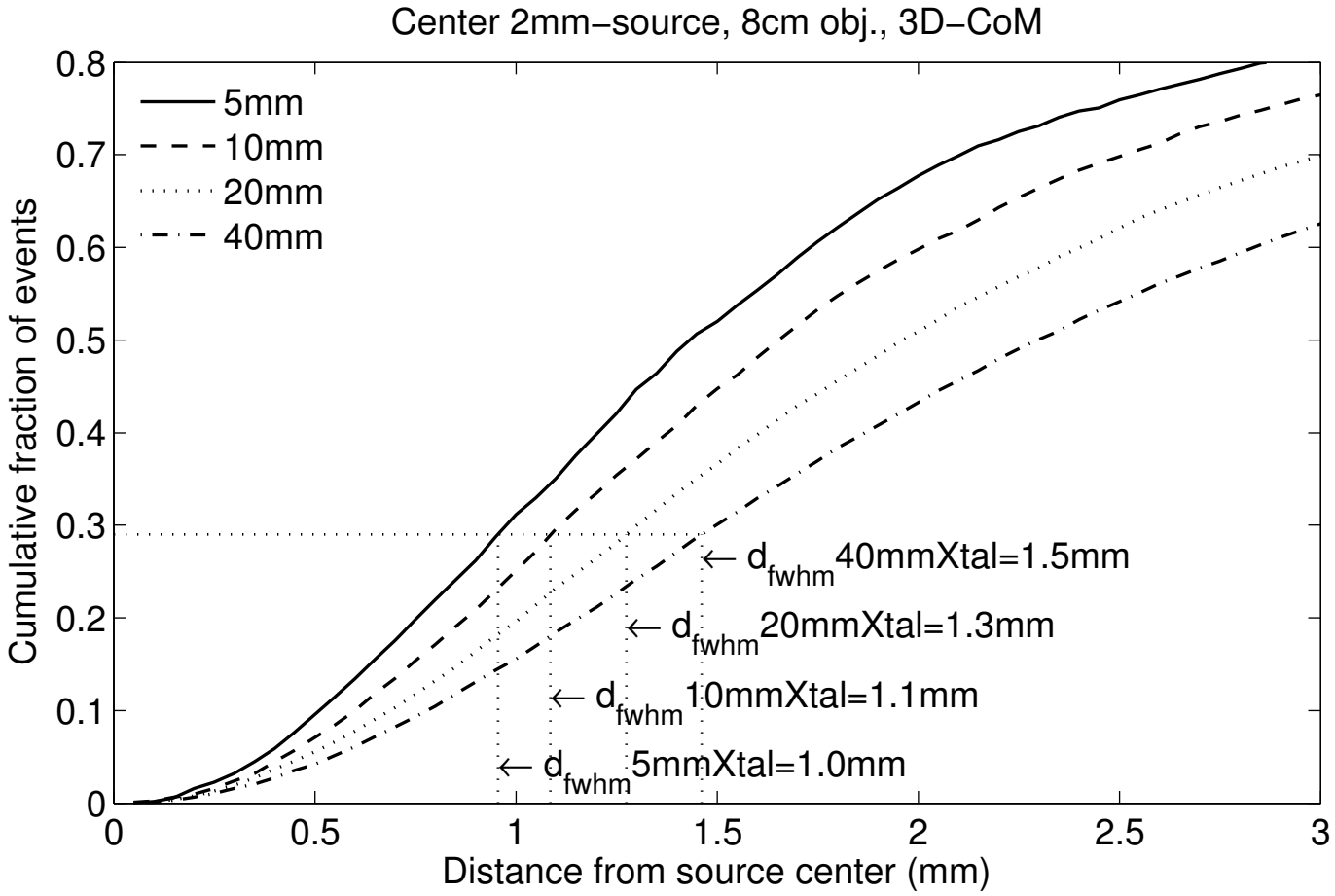
Center 2mm−source, 8cm obj., 3D−CoM
Cumulative fraction of events
Distance from source center (mm)
5mm
10mm
20mm
40mm
← d fwhm 40mmXtal=1.5mm
← d fwhm 20mmXtal=1.3mm
← d fwhm 10mmXtal=1.1mm
← d fwhm 5mmXtal=1.0mm
0
0.1
0.2
0.3
0.4
0.5
0.6
0.7
0.8
0
0.5
1
1.5
2
2.5
3

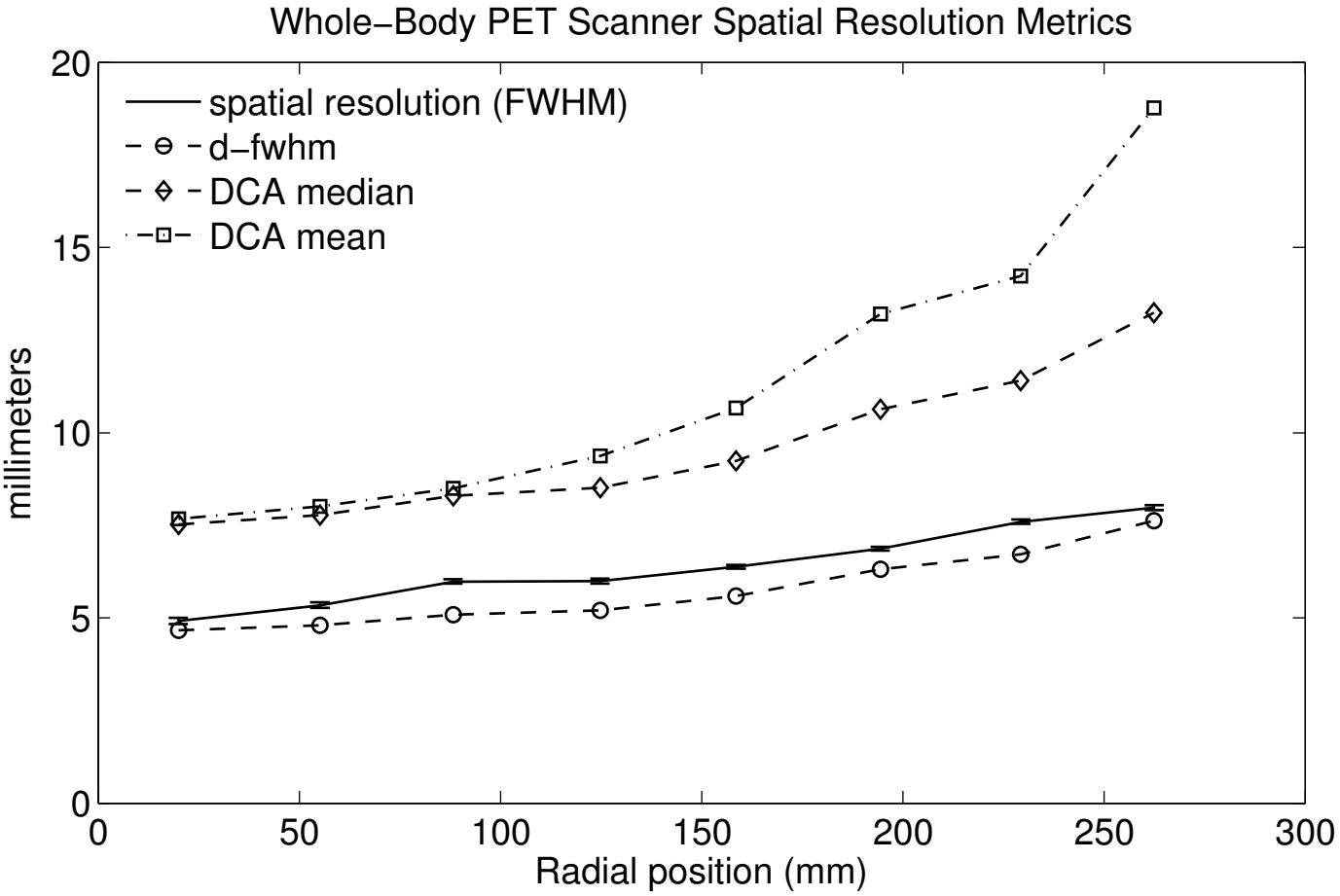
Whole−Body PET Scanner Spatial Resolution Metrics
spatial resolution (FWHM)
d−fwhm
DCA median
DCA mean
millimeters
Radial position (mm)
0
5
10
15
20
0
50
100
150
200
250
300

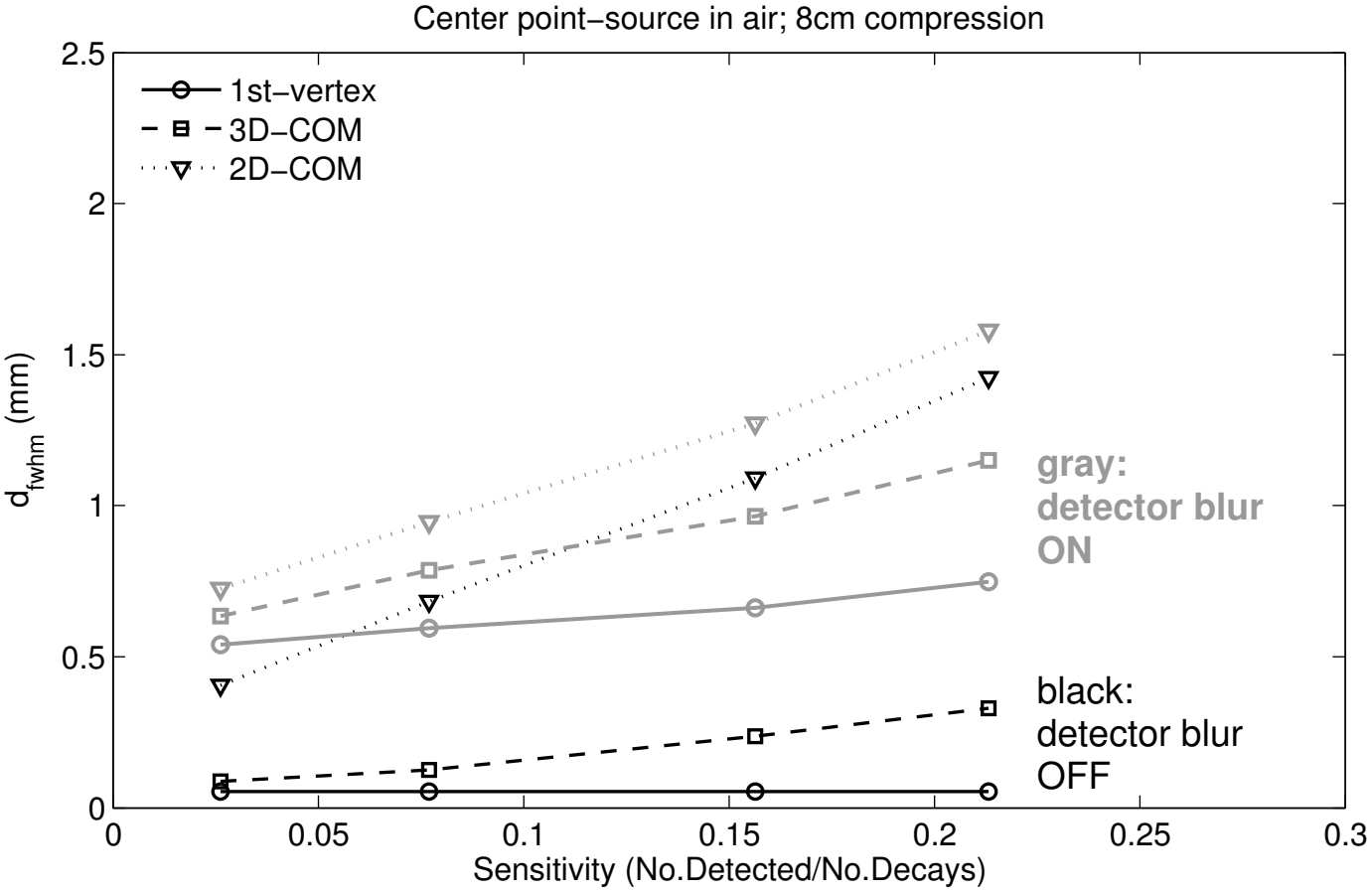
Center point−source in air; 8cm compression
1st−vertex
3D−COM
2D−COM
gray:
detector blur
ON
black:
detector blur
OFF
d_fwhm (mm)
Sensitivity (No.Detected/No.Decays)
0
0.5
1
1.5
2
2.5
0.05
0.1
0.15
0.2
0.25
0.3

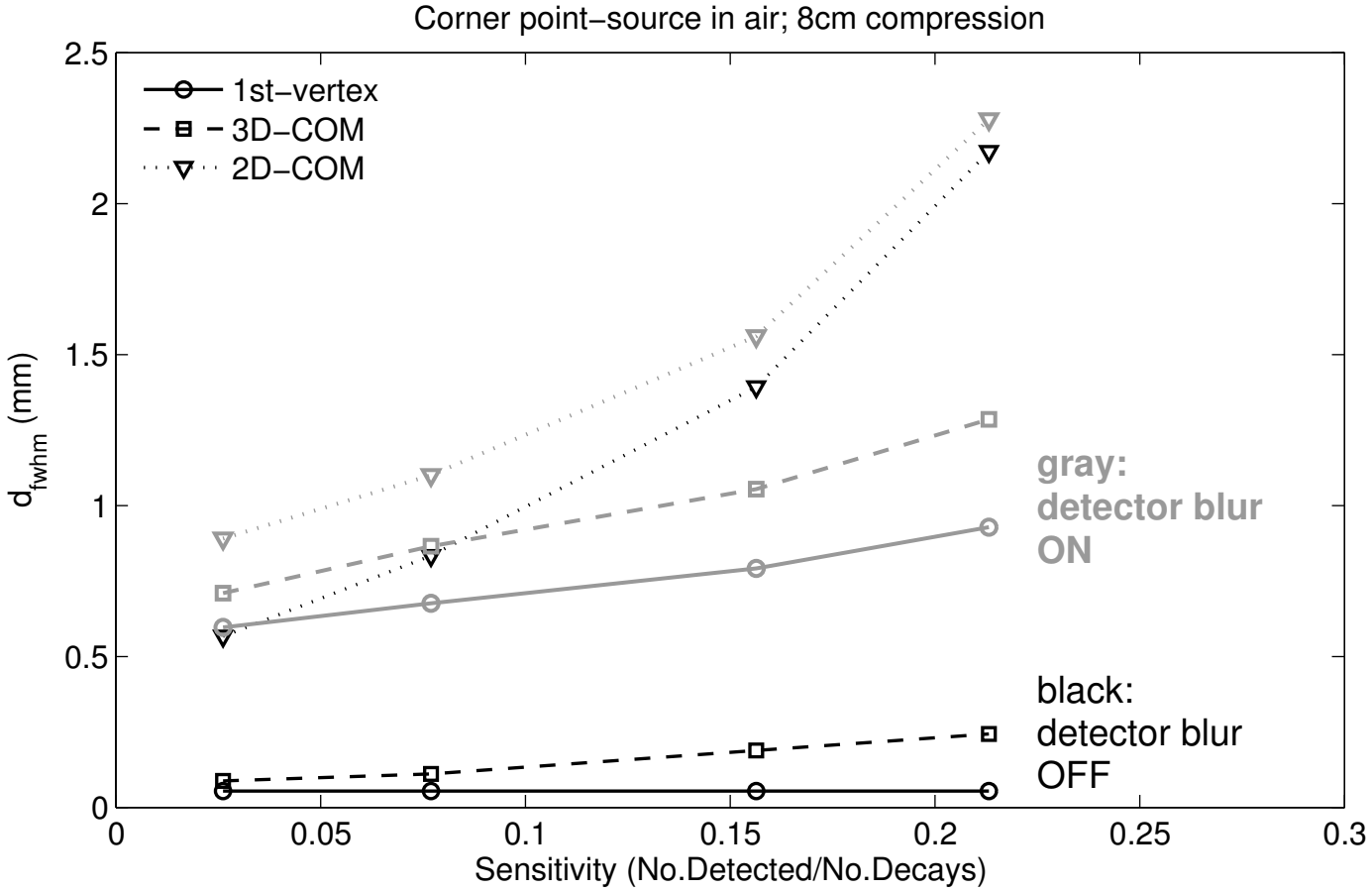
Corner point−source in air; 8cm compression
1st−vertex
3D−COM
2D−COM
gray:
detector blur
ON
black:
detector blur
OFF
d_fwhm (mm)
Sensitivity (No.Detected/No.Decays)
0
0.5
1
1.5
2
2.5
0.05
0.1
0.15
0.2
0.25
0.3

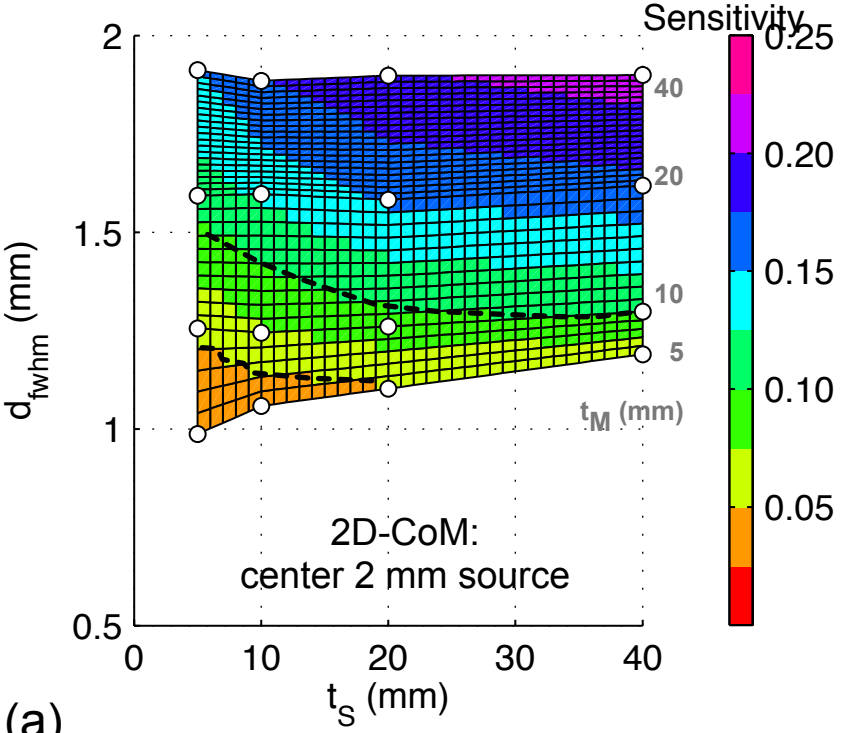
color=
Sensitivity
0.25
0.20
0.15
0.10
0.05
2
1.5
1
0.5
0
10
20
30
40
d_{fwhm} (mm)
t_S (mm)
t_M (mm)
40
20
10
5
2D-CoM:
center 2 mm source

(a)

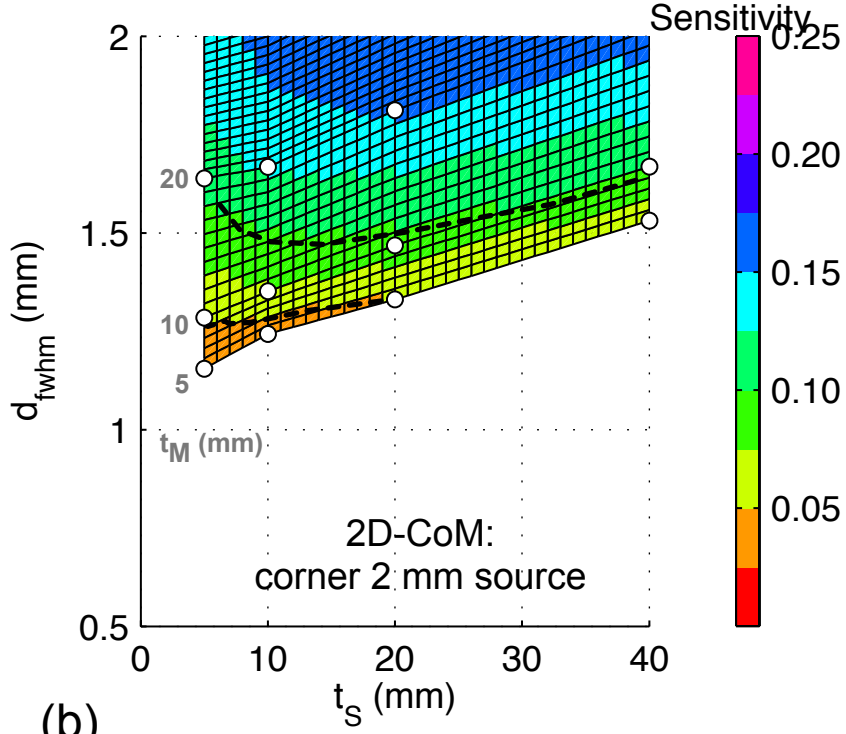
color=
Sensitivity
0.25
0.20
0.15
0.10
0.05
2
1.5
1
0.5
0
10
20
30
40
d_{fwhm} (mm)
t_S (mm)
t_M (mm)
20
10
5
2D-CoM:
corner 2 mm source

(b)

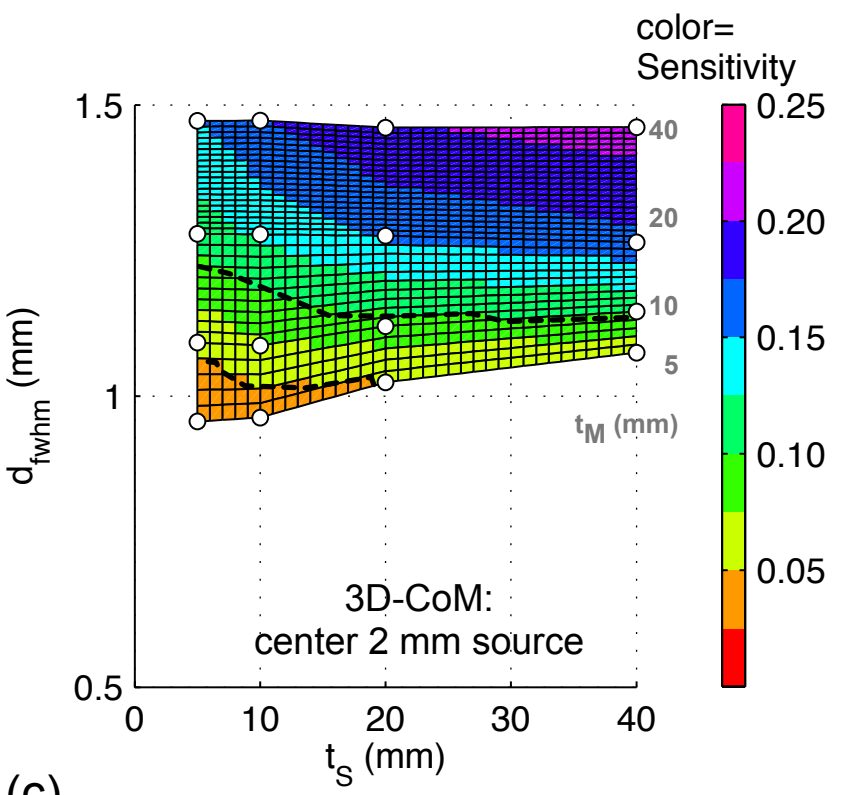
color=
Sensitivity
0.25
0.20
0.15
0.10
0.05
1.5
1
0.5
0
10
20
30
40
d_{fwhm} (mm)
t_S (mm)
t_M (mm)
40
20
10
5
3D-CoM:
center 2 mm source

(c)

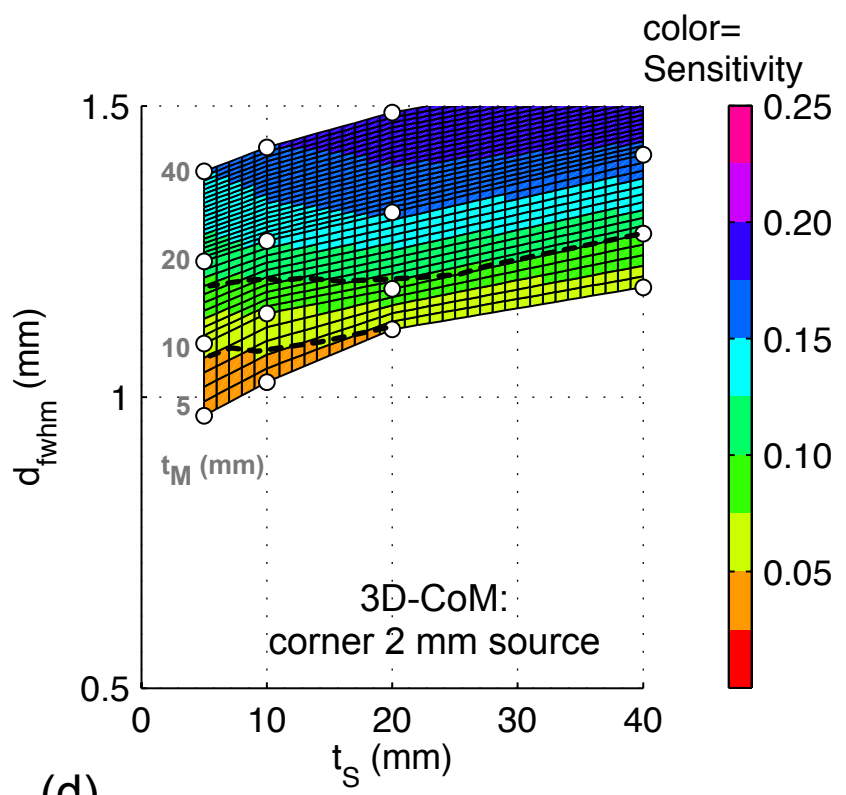
color=
Sensitivity
0.25
0.20
0.15
0.10
0.05
1.5
1
0.5
0
10
20
30
40
d_{fwhm} (mm)
t_S (mm)
t_M (mm)
40
20
10
5
3D-CoM:
corner 2 mm source

(d)

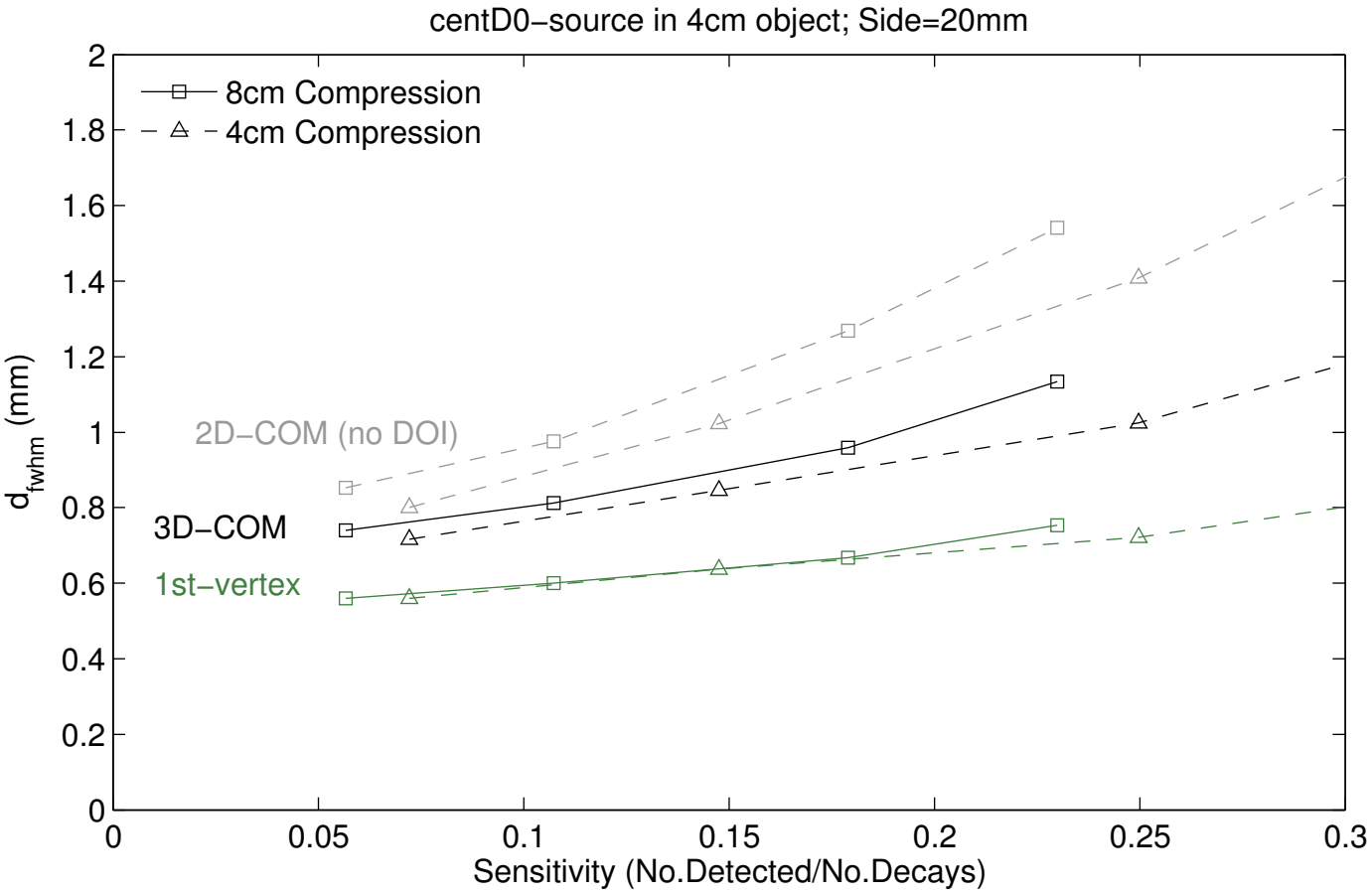
centD0−source in 4cm object; Side=20mm
8cm Compression
4cm Compression
2D−COM (no DOI)
3D−COM
1st−vertex
d_{fwhm} (mm)
Sensitivity (No.Detected/No.Decays)
0
0.2
0.4
0.6
0.8
1
1.2
1.4
1.6
1.8
2
0.05
0.1
0.15
0.2
0.25
0.3

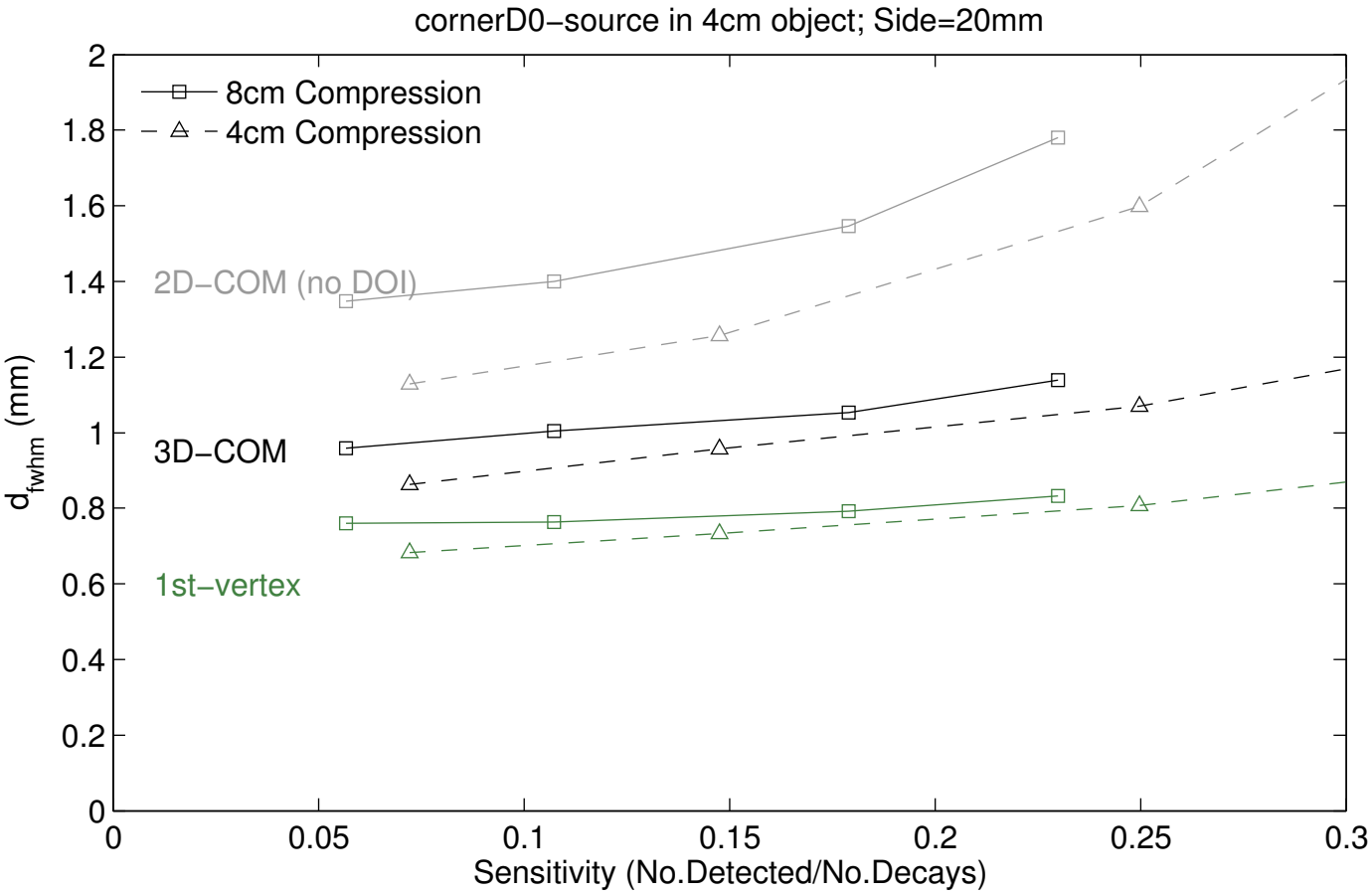
cornerD0−source in 4cm object; Side=20mm
8cm Compression
4cm Compression
2D−COM (no DOI)
3D−COM
1st−vertex
d_fwhm (mm)
Sensitivity (No.Detected/No.Decays)
0
0.2
0.4
0.6
0.8
1
1.2
1.4
1.6
1.8
2
0.05
0.1
0.15
0.2
0.25
0.3